

# Patterns of co-seismic strain computed from southern California focal mechanisms

Iain W. Bailey, Thorsten W. Becker and Yehuda Ben-Zion

Department of Earth Sciences, University of Southern California, Los Angeles, CA, USA. E-mail: iwbailey@usc.edu

Accepted 2008 December 24. Received 2008 December 22; in original form 2008 February 29

## SUMMARY

Geometrical properties of an earthquake population can be described by summation of seismic potency tensors that provide a strain-based description of earthquake focal mechanisms. We apply this method to  $\sim 170\,000$  potency tensors for  $0 < M_L \leq 5$  southern California earthquakes recorded between January 1984 and June 2003. We compare summed tensors for populations defined by faulting region and earthquake magnitude to investigate the relation between earthquake characteristics, tectonic domains and fault-related length scales. We investigate spatial scales ranging from  $\sim 1$ –700 km and use the results to identify systematic differences between seismic behaviour for different faults and different regions. Our results show features that are indicative of both scale-invariant and scale-dependent processes. On the largest scale the overall potency tensor summation for southern California  $0 < M_L \leq 5$  earthquakes over  $\sim 20$  yr corresponds closely to a double-couple (DC) mechanism with slip direction parallel to relative plate motion. The summed tensors and derived quantities for the different regions show clear persistent variations that are related to the dominant tectonic regime of each region. Significant differences between the non-DC components of the summed tensors, which we relate to fault heterogeneity, indicate systematic differences in deformation associated with earthquake populations from different fault zones or different magnitude ranges. We find an increase of heterogeneity for populations of smaller earthquakes and for regions where faulting deviates strongly from the overall sense of deformation, even when corrected for quality. The results imply an overall organization of earthquake characteristics into domains that are controlled to first order by geometrical properties of the largest faults and the plate motion. Smaller scale characteristics are related to local variations in the orientation, complexity and size of faults.

**Key words:** Spatial analysis; Earthquake dynamics; Earthquake source observations; Seismicity and tectonics; Dynamics and mechanics of faulting.

## 1 INTRODUCTION

This study is concerned with characterizing the geometrical properties of earthquake populations over multiple scales of magnitude and fault length based on focal mechanism observations. Theoretical studies of earthquakes and fault mechanics are typically based upon one of two end-member descriptions: homogeneous smooth faults in an elastic solid (e.g. Reid 1910; Rice 1980) or scale-independent faults with a fractal geometry (e.g. Kagan 1982; King 1983; Turcotte 1997). As summarized by Ben-Zion (2008), each case has very different implications for the mechanics of earthquakes, but both are simplistic in the sense that all faults are treated as belonging to a single dynamic regime. A wide variety of multidisciplinary observations indicate differences between fault structures and suggest an evolution with ongoing deformation, from highly disordered networks that have band-limited fractal properties toward dominant

connected structures that have relatively simple tabular geometries (Ben-Zion & Sammis 2003, and references therein). The limited amount and resolution of the available data present difficulties for studies aiming to clarify the geometrical properties of fault populations. In this paper we attempt to overcome these difficulties by performing multiscale and multisignal calculations, focusing on results that emerge from several different types of analysis.

Differentiating between classes of fault geometries can be approached by analysis of (i) surface fault traces (e.g. Wesnousky 1988; Stirling *et al.* 1996; Sagy *et al.* 2007), (ii) locations of earthquake hypocentres (e.g. Kagan & Knopoff 1980; Fehler *et al.* 1987; Nicholson *et al.* 2000; Holschneider & Ben-Zion 2006) and (iii) earthquake focal mechanisms (e.g. Kagan 1990; Amelung & King 1997; Hardebeck 2006; Twiss & Unruh 2007). Whereas fault traces are more representative of the long-term faulting processes than  $\sim 30$  yr of earthquake catalogue data, observations at the surface

may not correspond to processes at seismogenic depths. Locations of earthquake hypocentres sample faulting throughout the entire brittle crust, and recent advances in the computation of these locations (e.g. Waldhauser & Ellsworth 2000) have led to better resolution. The instrumental record is too short to provide a complete sampling of a given fault network, but data sets are now large enough to compare populations associated with different fault zones or tectonic domains. Focal mechanism catalogues contain fewer data than hypocentre catalogues due to limitations on the minimum number of instruments needed to compute a focal mechanism. However, representing earthquakes as point hypocentres neglects important geometrical information about the associated deformation (e.g. Libicki & Ben-Zion 2005). This study utilizes the information provided by focal mechanisms while maximizing the number of data, and in the following sections we present analyses of a catalogue based on  $\sim 170,000$  earthquakes. The data consist of  $0 < M_L \leq 5$  southern California earthquakes from the period January 1984–June 2003, and the large number of events allows us to investigate geometrical properties at multiple spatial scales in the range  $\sim 1$ –700 km. By representing individual focal mechanisms as seismic potency tensors (the strain-based equivalent of the moment tensor), we are able to describe geometrical properties of earthquake populations by summations of potency tensors (Kostrov 1974).

Potency tensor summations or analogous moment tensor summations have been used in previous studies by, for example, Fischer & Jordan (1991) to study the subducting Tonga slab, Amelung & King (1997) for northern California, Sheridan (1997) for the San Jacinto fault zone and Sipkin & Silver (2003) for aftershock sequences in southern California. Amelung & King (1997) and Sheridan (1997) illustrated the dominant effect of large ( $\sim 50$ –100 km) faults in a given region with respect to the summed tensor orientations, which have principle strain axes consistent with the fault orientations regardless of the magnitude range used for summation. Large faults of similar scales have also been shown to be important to stress inversion results by Hardebeck & Michael (2004) and Becker *et al.* (2005). When the summation region was expanded to a plate boundary scale, Amelung & King (1997) observed further that principle strain axes orientations are consistent with plate tectonic motions for nearly all magnitude ranges, implying that small earthquakes collectively deform the crust in the same way that large earthquakes do. Plate tectonic scales were also shown to be important to the properties of summed moment tensors by Fischer & Jordan (1991) and Sipkin & Silver (2003). Due to the persistent orientations of summed tensors for earthquakes in different magnitude ranges, Amelung & King (1997) interpreted their results as self-similar behaviour of all earthquake populations implying scale-invariant deformation processes. However, consistent orientations may also be explained by sets of relatively homogeneous deformation within finite scales associated with the large faults. Such length-scale dependence indicates a deviation from self-similar behaviour, which can be illustrated by showing that there are differences between the deformational patterns of large individual fault zones or tectonic domains.

As in previous studies, we find that the principle strain axes of summed tensors are aligned consistently with faulting directions for a range of different magnitude earthquakes. However, examining the non-double-couple (non-DC) component of the summed tensors indicates that the population geometries cannot be considered to be similar for different regions and magnitude bins. The non-DC component of the summed tensors can be interpreted as a measure of fault heterogeneity reflecting mixing of faulting styles within the sample, and we find that some regions show greater mixing

of faulting styles than others. Furthermore, there is a tendency for populations of larger magnitude earthquakes to behave more homogeneously than smaller magnitude populations in the same region, which can be related to the existence of faulting structures with varying levels of geometrical heterogeneity. Treating earthquake and fault-related systems as self-similar processes is therefore an inadequate description, since an earthquake population associated with a particular fault-related length-scale can have distinct characteristics. The overall patterns that we observe can be explained by the interaction of processes with a wide range of spatial scales, from those of plate tectonic motions ( $\sim 700$  km) to large fault zones ( $\sim 50$ –250 km) to geometrical complexities such as fault step-overs and kinks ( $\sim 5$ –50 km).

To perform a thorough analysis of earthquake potency tensors in southern California we develop and implement several analysis techniques. In Section 2, we describe potency tensor quantities and details of the southern California data used. In Section 3, we use six sub-sections to illustrate our analysis methods and associated results. Concentrating on the largest spatial scale and using the entire southern California data set as an example, we explain our two methods of tensor summation and how we interpret the results of these summations in Section 3.1. We then examine characteristics of deformation for different sized earthquakes by comparing summed tensors for different magnitude subsets in Section 3.2. A second spatial scale related to large fault zones is examined using regional subsets of the data in Section 3.3, and we partition these data sets by magnitude in Section 3.4. In Section 3.5, we investigate the robustness of our results and effects of data uncertainties by analysis of higher quality catalogues. Our smallest spatial scale is investigated in Section 3.6, where we outline additional methods for investigating spatial patterns at a 1 km scale for two regions, defining two new metrics and a method for assessing robustness to aid the interpretation of results. A discussion of our results is presented in Section 4.

## 2 THEORETICAL BACKGROUND AND DATA

### 2.1 The seismic potency tensor

The properties of the inelastic deformation in the earthquake source region can be described by the seismic potency tensor,  $P_{ij}$ , which is formally defined as

$$P_{ij} = \int_{V^s} \varepsilon_{ij}^p dV^s, \quad (1)$$

where  $\varepsilon_{ij}^p$  is the transformational strain tensor and  $V^s$  is the source volume (e.g. Ben-Zion 2003). The subscripts  $i$  and  $j$  denote the three Cartesian axis directions, and we take the convention that  $x_1$  points east,  $x_2$  points north and  $x_3$  points up. The transformational strain refers to the irreversible deformation that resets the zero reference level of the elastic stress during a given earthquake failure (Eshelby 1957). The seismic moment tensor,  $M_{ij}$ , can be computed from  $P_{ij}$  by  $M_{ij} = \sum_{k,l} c_{ijkl}^s P_{ij}$ , where  $c_{ijkl}^s$  is the tensor of elastic moduli for the source region. However,  $c_{ijkl}^s$  is poorly constrained for the space–time domains associated with earthquakes (e.g. Ben-Zion 2001; Ben-Zion 2003), and it does not affect the seismic radiation in the surrounding elastic solid (Woodhouse 1981; Ben-Zion 1989; Heaton & Heaton 1989; Ampuero & Dahlen 2005). We therefore prefer to use  $P_{ij}$  and related strain quantities, which make no assumptions about material properties at the source, rather than the more commonly used  $M_{ij}$ .

Assuming zero net torque and zero net rotation, both  $P_{ij}$  and  $M_{ij}$  are symmetric ( $P_{ij} = P_{ji}$ ) and have six-independent components (Aki & Richards 2002). Changes in volume due to regular tectonic earthquakes are typically considered to be negligible and we make this assumption in our study, constraining all potency tensors to be deviatoric such that  $P_{11} + P_{22} + P_{33} = 0$ . A deviatoric  $P_{ij}$  can be decomposed into a summation of DC and compensated linear vector dipole (CLVD) parts (Knopoff & Randall 1970; Jost & Hermann 1989). Whereas the DC component can be associated with slip on a planar surface, the CLVD component corresponds to compensated uniaxial compression or extension of a volume which requires a more complicated faulting geometry. Although it is generally accepted that many tectonic earthquakes contain a non-zero CLVD component (Julian *et al.* 1998), this is considered to be a second-order feature and not well constrained by inversion (Frohlich & Davis 1999). We therefore assume that it is appropriate to use potency tensors with zero CLVD component to represent the individual small ( $M_L \leq 5$ ) earthquakes used in this study. Potency tensors used to represent populations of earthquakes are computed by summation of DC tensors (Section 3.1) and will not necessarily have a zero CLVD component. In such a case, the relative size of the CLVD component indicates a degree of fault heterogeneity that implies a mixing of different faulting regimes. We describe this heterogeneity more specifically in Section 3.1.

The size of a potency tensor is given by the scalar potency,

$$P_0 = \sqrt{2P_{ij}P_{ij}} = \|P_{ij}\|, \quad (2)$$

which is related to slip,  $\Delta u$ , on a surface,  $A$ , by

$$P_0 = \int_A \Delta u \, dA. \quad (3)$$

The scalar potency can be used to compute the source mechanism tensor (Riedesel & Jordan 1989),

$$\hat{P}_{ij} = \sqrt{2} \frac{P_{ij}}{P_0}, \quad (4)$$

which has unit Euclidean norm and is used in this study to describe the orientation part of the potency tensor.

## 2.2 DC potency tensor catalogue

Our data set is based on a catalogue of focal mechanisms generated using the *HASH* algorithm (Hardebeck & Shearer 2002) for southern California earthquakes with  $M_L > 0$  in the period January 1984 to June 2003. This is an extended version of a catalogue available via the Southern California Earthquake Data Center (Hardebeck *et al.* 2005). In our catalogue, initial quality restrictions for the required station distribution are relaxed, to increase the number of data (J. Hardebeck, private communication, 2006). Maximization of the number of data results in an increased number of less well-constrained focal mechanisms, but we assume that there will be no significant bias in average focal mechanism properties. The catalogue generated by *HASH* contains mechanism quality estimates that take into account the sensitivity of the inversion to both the station distribution and velocity model.

Rearranging eq. (4), the potency tensor is given by  $P_{ij} = P_0 \hat{P}_{ij} / \sqrt{2}$ . We compute  $\hat{P}_{ij}$  from the fault plane solutions using geometrical transformations described in Appendix A, and  $P_0$  using the magnitude-potency scaling relation of Ben-Zion & Zhu (2002),

$$\log_{10} P_0 = 0.0612M_L^2 + 0.988M_L - 4.87, \quad (5)$$

where  $P_0$  has units of  $\text{km}^2 \text{ cm}$ , and  $M_L$  is the local magnitude obtained from the catalogue.

The inversion of seismic data for a DC mechanism assumes that the seismic radiation originates from a single point source. For a circular crack of radius  $r$ , the scalar potency scales as  $P_0 = c\Delta\epsilon_s r^3$  (Eshelby 1957; Ben-Zion 2003), where  $\Delta\epsilon_s$  is the static strain drop and  $c$  is  $16/7$  for an infinite Poissonian solid. Combining this with eq. (5) and assuming that  $\Delta\epsilon_s = 1 \times 10^{-4}$ , we estimate the rupture dimension of the largest employed earthquakes with  $M_L = 5.0$  as  $r \sim 1.2$  km. Thus, at the scales used in this study the point source approximation is generally appropriate for earthquakes with  $M_L \leq 5$  ( $P_0 \leq 1.6 \text{ km}^2 \text{ cm}$ ), and larger events are removed from the catalogue.

Errors associated with calculation of the orientation part of the focal mechanism introduce the largest uncertainty into the potency tensor parameters. We therefore interpret the focal mechanism inversion stability as a measure of potency tensor quality and consider errors related to the measurement of  $M_L$  and computation of  $P_0$  as negligible. By applying the *HASH* inversion to first motion data in a region where the faulting structures are well studied, Kilb & Hardebeck (2006) inferred that the most reliable estimates of quality are the focal mechanism probability (PROB), which records the proportion of acceptable solutions within  $30^\circ$  of the preferred solution, and fault plane uncertainty (FPU), which records the RMS angular difference of acceptable solutions from the preferred solution. Both PROB and FPU are used in this study. According to the *HASH* output, location errors are such that 98.5% of horizontal errors and 92% of vertical errors are smaller than 1 km. Since we do not perform spatial analyses at scales smaller than 1 km, we do not relocate events. Further details about our potency tensor catalogue, which contains 169, 866 events, are provided in Table 1. Locations of the earthquakes are shown in Fig. 1.

## 3 ANALYSIS

### 3.1 Summed potency tensors

#### 3.1.1 Quantities computed and physical interpretations

For a population of  $N$  earthquakes, the combined potency tensor can be calculated by a potency tensor summation,

$$P_{ij}^{TOT} = \sum_{k=1}^N P_{ij}^{(k)}. \quad (6)$$

The associated inelastic strain for a volume including the earthquakes,  $V$ , is given by  $P_{ij}^{TOT}/(V)$ , and the mean rate of deformation due to the earthquakes over a time period,  $\Delta t$ , is given by  $P_{ij}^{TOT}/(V\Delta t)$ . Kostrov (1974) defines these quantities in terms of  $M_{ij}$ , and uses a factor of  $1/(2\mu)$ , where  $\mu$  is rigidity, to account for elastic properties of  $V$ . In a population with a wide range of earthquake sizes,  $P_{ij}^{TOT}$  is likely to be dominated by the largest earthquakes, so advantages provided by a large number of small events, such as the lesser influence of outliers and greater spatial sampling of a region, are somewhat diminished. It is therefore also useful to examine summations of source mechanism tensors. The source mechanism summation is given by

$$P_{ij}^{SM} = \sum_{k=1}^N \hat{P}_{ij}^{(k)}. \quad (7)$$

The summation in eq. (7) is not influenced by individual earthquake sizes, so an analysis of the two different normalized tensors,

**Table 1.** Summary of the earthquake data set used in this study, which contains 169,866 events. FPU and PROB correspond to measures of focal mechanism quality (Hardebeck & Shearer 2002).

Number of events	169,866
Source data	SCSN polarity data (available at <a href="http://www.scecdc.scec.org/STP/stp.html">http://www.scecdc.scec.org/STP/stp.html</a> )
Location method	<i>SIMULPS</i> (Thurber 1983)
Minimum no. stations for inversion	5
No. inversions using <i>S</i> -wave arrivals	21,700
No. multiple solutions removed	30,646 (based on value of PROB)
No. large events ( $M_L > 5$ ) removed	56
Time period covered	01/01/1984–2/6/2003
Longitude range	113.96–121.66°W (~690 km)
Latitude range	31.63–37.89°N (~720 km)
Depth range	0–15 km
$M_L$ range	0.01–5.00 ( $1.34 \times 10^{-5} < P_0 \leq 3.98 \times 10^1 \text{ km}^2 \text{ cm}$ )
FPU range	11–64°
PROB range	0.09–1.00

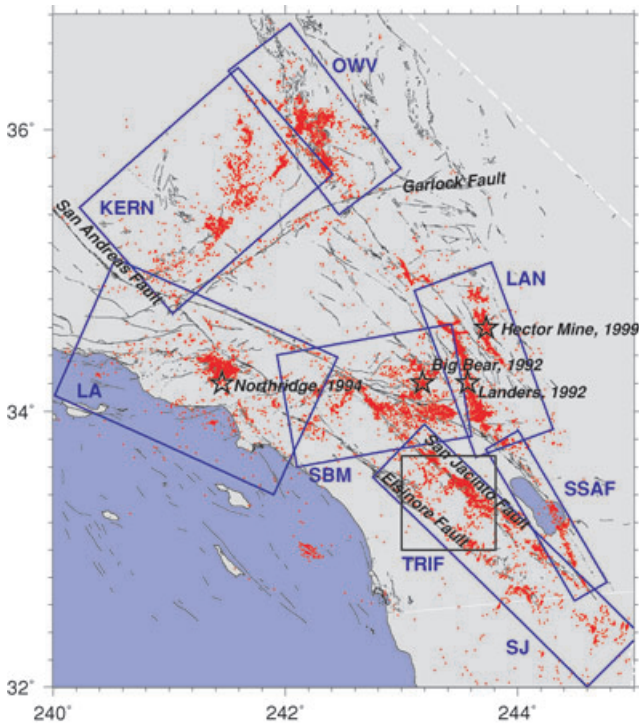


**Figure 1.** Red dots show the locations of earthquake focal mechanisms used in this study. Major Faults are shown by black lines based on Jennings (1975). Blue rectangles denote sub-regions outlining distinct regions of seismicity which are used for spatial analysis of potency tensor summations: Owens Valley (OWV), Kern County (KERN), Los Angeles Basin (LA), Landers and Hector Mine rupture areas (LAN), San Andreas and San Jacinto junction in the San Bernardino Mountains (SBM), San Jacinto and Elsinore faults (SJ), and Salton Sea area of the San Andreas (SSAF). The  $75 \times 75$  km region TRIF, marked by a black outline, is used for detailed spatial analyses. Though not included in the analysis, hypocentres of notable large earthquakes are marked for reference.

$\hat{P}_{ij}^{TOT} (= P_{ij}^{TOT} / \|P_{ij}^{TOT}\|)$  and  $\hat{P}_{ij}^{SM} (= P_{ij}^{SM} / \|P_{ij}^{SM}\|)$ , allows us to compare the orientation of the total earthquake potency with the average orientation properties of the population. Standard stress inversions (e.g. Angelier *et al.* 1982; Michael 1987) weight earthquake focal mechanism data equally regardless of magnitude, and so are more analogous to  $\hat{P}_{ij}^{SM}$  than  $\hat{P}_{ij}^{TOT}$ , though we emphasise

that we are calculating the strain rather than inverting for the most likely stress.

The interpretation of a normalized summed potency tensor can be aided by separating its four remaining degrees of freedom into three describing the orientation of the principle strain axes and one describing the size of the CLVD component. The principle strain axes are given by the eigenvectors,  $\mathbf{e}_1$ ,  $\mathbf{e}_2$  and  $\mathbf{e}_3$ , of  $P_{ij}$ , which correspond to the maximum compressive (*P*) axis, the intermediate (*B*) axis and the maximum extensive (*T*) axis, respectively. Taking a convention of compression being negative, the corresponding eigenvalues are given by  $\lambda_1 \leq \lambda_2 \leq \lambda_3$ . For a DC potency tensor,  $\lambda_2 = 0$ , and as such the value of  $\lambda_2$  relates directly to the size of the CLVD component (further details are given in Appendix B). In this study, we quantify the CLVD component by the ratio (Julian *et al.* 1998),

$$r_{\text{CLVD}} = \frac{\sqrt{6}}{2} \lambda_2, \quad (8)$$

which ranges between the two pure CLVD cases of  $r_{\text{CLVD}} = -0.5$  and  $0.5$ , via the pure DC case of  $r_{\text{CLVD}} = 0$ . The factor 2 is a matter of convention, since a pure CLVD mechanism may also be described by the summation of two separate DC components with orientations differing by  $90^\circ$ . Alternative quantification of the CLVD size for a normalized deviatoric tensor is given by the Gamma-index (Kagan & Knopoff 1985),  $\Gamma = -(3/2)\sqrt{6} \lambda_1 \lambda_2 \lambda_3$ , or  $f_{\text{CLVD}} = -\lambda_2 / \max(|\lambda_1|, |\lambda_3|)$  (Giardini 1984), which also range between  $-0.5$  and  $0.5$  and are compared to  $r_{\text{CLVD}}$  in Appendix C.

The orientation of the strain axes relates to the dominant direction of faulting, whereas the value of  $r_{\text{CLVD}}$  describes the nature of deformation that cannot be explained by the dominant fault orientation, thus indicating a degree of heterogeneity in DC orientations. Since the CLVD component will be zero for summations of DCs where (i) all *B*-axes are parallel, (ii) all fault planes are parallel or (iii) all slip vectors are parallel (Julian *et al.* 1998; Kagan 2009), its existence indicates a departure from simple fault geometries. Furthermore, the CLVD component will tend to be zero for summations of random fluctuations about a dominant DC orientation, since variations in one direction will generally be cancelled out by variations in the opposite sense (this is illustrated by simulations of uniformly random DC orientations in Appendix D). For example, if the dominant deformation is consistent with pure strike-slip faulting, equal second-order contributions of reverse and normal faulting will result in  $r_{\text{CLVD}} = 0$ . If the second-order contributions are not equal such that there is more potency released by normal faulting

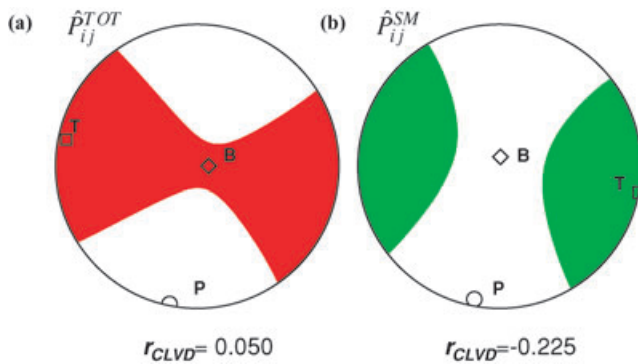


**Figure 2.** Results of (a) a normalized potency tensor and (b) a normalized source mechanism tensor based on summation for the entire southern California data set of  $0 < M_L \leq 5$  earthquakes. These plots show lower hemisphere, equal area projections, such that orientations where the strain is extensive are coloured and orientations where the strain is compressive are white. The orientations of the three principal strain axes are overlain as open symbols ( $P$ -axis = circle,  $B$ -axis = diamond and  $T$ -axis = square). Labels for the axes are shown next to each symbol. Beneath each plot, we display the value of  $r_{CLVD}$  which quantifies the size of the CLVD component in each of the summed tensors.

mechanisms than reverse faulting mechanisms  $r_{CLVD} < 0$ , whereas the opposite case leads to  $r_{CLVD} > 0$ . A CLVD component therefore requires the existence of fault heterogeneity as well as asymmetry within that heterogeneity. The specific fault heterogeneity that may lead to a given CLVD component is not uniquely defined by focal mechanism data since the slip direction also depends upon the details of the fault loading.

### 3.1.2 Southern California summation results

Strain axes orientations and the size of the CLVD component can be displayed by a ‘beachball plot’, as in Fig. 2 for the two summations over the entire  $0 < M_L \leq 5$  southern California data set. The downward pointing orientations of the principle strain axes are shown using open symbols, whereas the CLVD size is indicated by the departure of the plot from a pure DC, for which case the two white and non-white regions would intersect in the direction of the  $B$  axis.

In Fig. 2, both plots show near vertical  $B$ -axes close to the middle of the circle, whereas the horizontal  $P$ - and  $T$ -axes plot close to the edge. This implies a dominance of strike-slip faulting in both number of earthquakes ( $\hat{P}_{ij}^{SM}$ ) and the combined potency release ( $\hat{P}_{ij}^{TOT}$ ). From a given set of principle strain axes, an associated fault plane and auxiliary plane for the DC component are described by normal vectors that are  $45^\circ$  between the  $P$ - and  $T$ -axes, which can be converted to fault strike and dip angles via simple geometrical relations (e.g. Stein & Wysession 2003, p. 218). The corresponding slip direction can then be found by resolving the  $T$ -axis onto each of the possible fault planes. For  $\hat{P}_{ij}^{TOT}$  in Fig. 2, the  $P$ - and  $T$ -axis orientations would be consistent with left-lateral slip on a fault with strike  $56^\circ$  and dip  $87^\circ$ , or right-lateral slip on a fault with strike  $-34^\circ$  and dip  $86^\circ$ . Neither are consistent with the section of the right-lateral San Andreas Fault shown in Fig. 1, which has a strike largely in the range  $\sim -67^\circ$  to  $-61^\circ$  before bending to  $\sim -45^\circ$  in the northwest of the region. The left-lateral Garlock Fault has a more consistent strike in the range  $\sim 57^\circ$  to  $90^\circ$ . The axis orientations in Fig. 2 are consistent with relative plate motion directions given by the NNR-NUVEL-1A model (DeMets *et al.* 1994), where in the

southern California region the Pacific Plate moves relative to North America with an azimuth in the range  $\sim -35^\circ$  to  $-41^\circ$ .

### 3.1.3 Comparison of summed tensors

To quantify the difference in orientation of the strain axes, we consider the minimum angle,  $\Omega$ , required to rotate about any pole from one orientation of  $P$ -,  $B$ - and  $T$ -axes to another. Given axial symmetries, the maximum value of  $\Omega$  is  $120^\circ$ . We calculate  $\Omega$  using an algorithm outlined by Kagan (1991) and the relevant equations are given in Appendix E. This angle is called  $\Omega_{sd}$  by Frohlich & Davis (1999). For the two summation types shown in Fig. 2,  $\Omega = 7.6^\circ$ , reflecting the small difference between the dominant faulting styles. The significance of this similarity, despite the difference in summation type, is highlighted in Fig. 3, which shows that the varying contribution of earthquakes from different magnitude bins is related to a typical Gutenberg–Richter distribution. It is clear that the potency tensor summation,  $\hat{P}_{ij}^{TOT}$  is dominated by events in the largest ( $4 < M_L \leq 5$ ) magnitude bin. The source mechanism summation is based on normalized tensors, and hence dominated by more numerous events in the  $1 < M_L \leq 2$  range. Based on inspection of the frequency–magnitude conformance to a Gutenberg–Richter distribution, the magnitude of completeness is close to 1 in the focal mechanism catalogue, and earthquakes in the range  $0 < M_L \leq 1$  are therefore under-represented.

Whereas the strain axes orientations are similar for the two summation types in Fig. 2, the CLVD components are different. For  $\hat{P}_{ij}^{SM}$ ,  $r_{CLVD} = -0.225$  and the negative sign indicates compression in the direction of the  $B$ -axis. Since the  $B$ -axis is vertical, this implies that normal faulting mechanisms mix with the dominating strike-slip mechanisms in the earthquake population. For  $\hat{P}_{ij}^{TOT}$ ,  $r_{CLVD} = 0.050$ , indicating a slightly larger contribution of reverse faulting than normal faulting in the background of the overall strike-slip deformation. We compute uncertainties for the values of  $r_{CLVD}$  by bootstrap re-sampling of the summed tensor, using the method described by Press *et al.* (1992, p. 691). We resample each summed tensor and compute  $r_{CLVD}$  10 000 times to produce a density distribution for  $r_{CLVD}$  and from this calculate the 95% confidence interval for the quantity. In the case of  $\hat{P}_{ij}^{SM}$ , the confidence limits are  $[-0.230, -0.220]$ , implying a robust CLVD component. For  $\hat{P}_{ij}^{TOT}$ , the 95% confidence limits are  $[-0.028, 0.128]$ , indicating that there is no strong evidence that  $\hat{P}_{ij}^{TOT}$  is different from a pure DC mechanism. With regard to the result for  $\hat{P}_{ij}^{SM}$ , summations of simulated random DC orientations in Appendix D indicate that  $r_{CLVD} > |0.225|$  in  $\sim 34\%$  of cases, but random fluctuations cannot explain the consistent strain axes orientations for the two summations. If we consider both CLVD results to be non-random, the discrepancy implies that the crustal thinning caused by a large number of normal faulting earthquakes in southern California has been cancelled out by reverse faulting earthquakes which are less common but have higher magnitudes. As will be shown in Section 3.3, the majority of this reverse fault component exists in the Los Angeles Basin (LA).

The results of the bootstrap analyses in this and subsequent sections suggest uncertainties that are larger for  $\hat{P}_{ij}^{TOT}$  than for  $\hat{P}_{ij}^{SM}$ . This is due to the sensitivity of  $\hat{P}_{ij}^{TOT}$  to a small number of large earthquakes within the population. The bootstrap analysis does not take into account the variation in quality of individual mechanisms, and we address this in separate quality analyses (Section 3.5).

We can isolate the total geometrical differences between two normalized tensors,  $\hat{P}_{ij}^A$  and  $\hat{P}_{ij}^B$ , using the angular measure (Frohlich

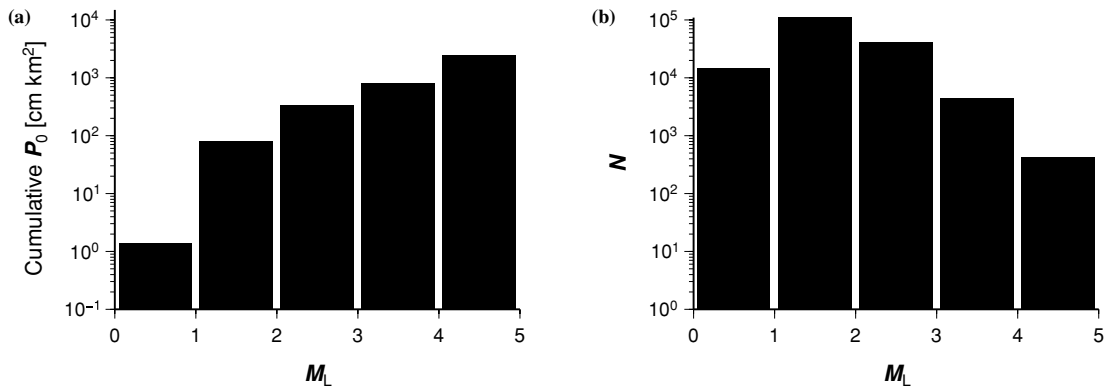


**Figure 3.** Histograms of (a) the summed scalar potency and (b) the number of events for each magnitude bin using the entire data set.

& Davis 1999; Sipkin & Silver 2003),

$$\Theta = \arccos \left( \hat{P}_{ij}^A \hat{P}_{ij}^B \right), \quad (9)$$

which ranges from 0 to 180° and is called  $\Omega_{9n}$  by Frohlich & Davis (1999). This angle does not correspond to  $\Omega$ , which measures the difference in strain axes orientation, since it is defined in the space of normalized nine-component tensors, and hence is affected by the size of the CLVD components in both tensors. For two summed tensors with the same orientation of strain axes but  $r_{\text{CLVD}}$  values of 0 and 0.5,  $\Theta = 30^\circ$ . For the summations shown in Fig. 2,  $\Theta = 18^\circ$ .

We compute uncertainty bounds for both of the difference angles by simultaneous bootstrap re-sampling of the two summed tensors, computing  $\Omega$  and  $\Theta$  between a re-sampled  $\hat{P}_{ij}^A$  and a re-sampled  $\hat{P}_{ij}^B$  10 000 times. As in the bootstrap analysis of  $r_{\text{CLVD}}$ , we compute 95% confidence intervals based on the resulting distribution of both angles. This analysis gives a range of 4.7–12.0° for  $\Omega$  and 14.7–

22.0° for  $\Theta$ . By comparison, a bootstrap analysis of  $\hat{P}_{ij}^{\text{TOT}}$  for southern California indicates that 95% of the resampled summed tensors are within  $\Omega = 5.0^\circ$  and  $\Theta = 7.1^\circ$  of each other. Hence compared to the uncertainty of the summation results, the difference between  $\hat{P}_{ij}^{\text{TOT}}$  and  $\hat{P}_{ij}^{\text{SM}}$  is not that large in terms of orientation differences given by  $\Omega$ , but it is in terms of  $\Theta$  where the CLVD components are taken into account.

### 3.2 Summations over different magnitude bins

We investigate partitioning of the overall potency release into earthquakes of different magnitudes by separating the catalogue into five magnitude subsets, using the ranges:  $0 < M_L \leq 1$ ,  $1 < M_L \leq 2$ , ...,  $4 < M_L \leq 5$  and computing  $P_{ij}^{\text{TOT}}$  and  $P_{ij}^{\text{SM}}$  for each. Fig. 4 displays  $\hat{P}_{ij}^{\text{TOT}}$  and  $\hat{P}_{ij}^{\text{SM}}$  for each magnitude bin of the entire

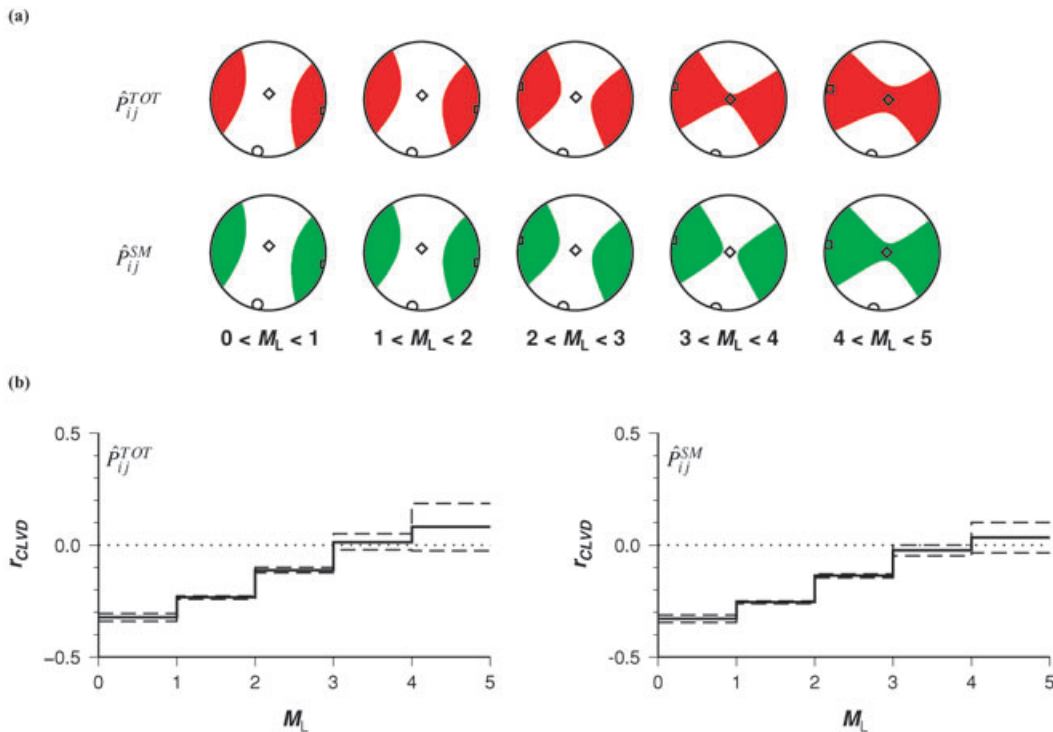


**Figure 4.** (a) Potency tensor and source mechanism tensor summations for magnitude subsets of our potency tensor data set. The radii of the beachballs are equal, such that these represent the normalized tensors,  $\hat{P}_{ij}^{\text{TOT}}$  and  $\hat{P}_{ij}^{\text{SM}}$  for each bin (rather than  $P_{ij}^{\text{TOT}}$  and  $P_{ij}^{\text{SM}}$ ). The  $P$ -,  $T$ - and  $B$ -axis orientations are overlain as in Fig. 2. (b) Values of  $r_{\text{CLVD}}$  for each magnitude bin in each of the summations plus 95% confidence intervals computed by bootstrap analysis.

catalogue, using the same representation as in Fig. 2. As suggested by the comparison of  $\hat{P}_{ij}^{TOT}$  with  $\hat{P}_{ij}^{SM}$  for the entire catalogue, we find that the orientations of the strain axes are very similar for different magnitude ranges (Fig. 4a). We have tested this in more detail by computing  $\Omega$  between all pairs of tensors for magnitude bins, and results are given in Appendix F. Based on 95% confidence limits given by bootstrap analyses, we find no evidence for principle strain axes orientation differences greater than  $7^\circ$ .

The CLVD component is larger and increasingly negative for lower magnitude bins (Fig. 4b) in both summation types. Given the constant strain axis orientations which imply strike-slip dominance, this suggests a tendency toward an increased normal faulting/vertical thinning component in smaller earthquakes. The values of  $r_{CLVD}$  suggest a change in the CLVD component with magnitude that is steady and outside of the 95% confidence limits from bootstrap analysis for any of the magnitude bins. The largest value of  $r_{CLVD}$  is 0.32 for the  $0 < M_L \leq 1$  bin, and although such a CLVD component was generated by  $\sim 20\%$  of random simulations, we would expect more variation in the principle axes orientations if the effect was due to randomness. Computation of  $\Theta$  between all pairs of tensors for magnitude bins and comparison of 95% confidence limits indicate robust differences between magnitude bins of up to  $20^\circ$  (Appendix F). This is in contrast to the same comparisons based on the angle  $\Omega$ , indicating that taking the CLVD component into account is necessary to show robust differences between summed tensors of different magnitude bins.

The persistence in the orientations of principle strain axes indicates that dominant faulting is the same for all earthquakes, but the CLVD differences highlight that the tensors are not self-similar and imply that the CLVD-related heterogeneity is greater for smaller earthquake populations.

### 3.3 Summations over different tectonic regions

To understand how the potency release of different fault zones contributes to the overall potency release, we compute  $P_{ij}^{TOT}$  and  $P_{ij}^{SM}$  for seven subregions outlined by polygons with dimensions  $\sim 50$ – $250$  km (Fig. 1). These polygons are subjectively chosen to outline regions of high seismicity and recognized faulting structures while minimizing the total number of regions used. In the following, we provide a brief qualitative summary of each region, though more quantitative analysis of the relative number and potency release of each region, as well as comparisons of the temporal seismic behaviour are given in Appendix G. The comparisons in the Appendix are removed from the strain-based focus of this study, but provide further support for distinct differences between the seismic behaviour of such large-scale tectonic domains.

Region SJ is largely dominated by seismicity associated with the San Jacinto and Elsinore Faults, both of which are NW trending strike-slip faults that may be considered complex due to their many branches, step-overs and gaps. The region contains one small aftershock sequence associated with the 1987 Superstition Hills earthquake, but is otherwise dominated by a fairly constant level of seismicity that conforms to a Gutenberg–Richter distribution. Region SSAF contains the most southern extent of the San Andreas Fault as well as the pull-apart basin of the Salton Sea. It is the smallest region considered and contributes the smallest amount of potency release and number of earthquakes to the southern California summed tensors in Section 2. Aftershocks of the 1987 Superstition Hills earthquake are present in both regions SJ and SSAF. Region LA

includes the Los Angeles Basin (dominantly compressional reverse faulting) as well as some of the surrounding seismicity (both left- and right-lateral strike-slip faults). Potency release in this region is dominated by aftershocks of the 1994 Northridge earthquake, which contribute relatively more to the southern California total potency release than to the total number of events. Region SBM includes the San Bernardino mountains, where the San Andreas fault bends to a more westerly strike and intersects the northern extent of the San Jacinto fault. Seismicity in the northeast of this region is dominated by aftershocks of the 1992 Big Bear earthquake. Region LAN is almost entirely dominated by aftershocks of the 1992 Landers and 1999 Hector Mine earthquakes, the two largest events occurring in the region during the time period of our catalogue. These aftershock sequences result in the region being the largest contributor of potency release to the entire catalogue. Both mainshocks may be considered as complex ruptures due to the multiple faults that sustained slip, and these features are also represented in the aftershocks. Region KERN includes a large component of seismicity where fault traces are not mapped in the Kern County/Lake Isabella area, which includes the southern edge of the Sierra Nevada. Hydrothermal activity is present in the region, which may relate to the large number of small normal faulting earthquakes that contribute little in terms of overall potency release. Region OWV includes the southern part of Owens Valley and the Coso geothermal region. Owens valley is bounded by large normal faults, but also contains a large strike-slip fault. The large amount of microseismic activity means that the region contributes more earthquakes to the catalogue than any other region, whereas the small size of these earthquakes leads to a total potency contribution that is only the fourth largest.

Fig. 5(a) shows the results of both potency tensor summation types for each of the seven regional subsets of our catalogue. In all results except  $\hat{P}_{ij}^{TOT}$  for region LA, the  $B$ -axis is the most vertical axis, indicating a dominance of strike-slip deformation at these  $\sim 50$ – $250$  km scales. Despite the consistent style of faulting, variations in the azimuth of  $P$ - and  $T$ -axes lead to distinct differences in the strain-axes orientations between different regions. We quantify these differences and show that they are robust by computing  $\Omega$  for all pairs of regionally summed tensors as well as 95% confidence intervals in Appendix F. From a visual comparison with the regional fault map, the  $P$ - and  $T$ -axis orientations are consistently close to  $45^\circ$  from the dominant fault strikes of each region, but rarely close to the orientations for the southern California summed tensors in Fig. 2. This indicates that for these regions, the dominant length scales underpinning the deformation have shifted from plate boundary scales to those of the largest nearby fault structure.

Fig. 5(b) shows that the nature of the CLVD component also varies strongly from region to region, indicating differences in the nature of fault heterogeneity within them. All regions except SBM have a larger absolute CLVD component than that of the entire region for the source mechanism summations, and in general the absolute  $r_{CLVD}$  value is smaller for  $\hat{P}_{ij}^{TOT}$  than  $\hat{P}_{ij}^{SM}$ . Of the different regions, LA is the only case where  $r_{CLVD}$  is positive, implying that the small positive CLVD component of  $\hat{P}_{ij}^{TOT}$  for the entire southern California region results largely from reverse faulting in the Los Angeles region. The other regions have a greater tendency for normal faulting, though the larger  $|r_{CLVD}|$  values for  $\hat{P}_{ij}^{SM}$  suggest that this tendency is greater for smaller magnitude earthquakes. In general, the CLVD components are highest in the regions where the axes orientations are most different from those of southern California as a whole (i.e. KERN and LA).

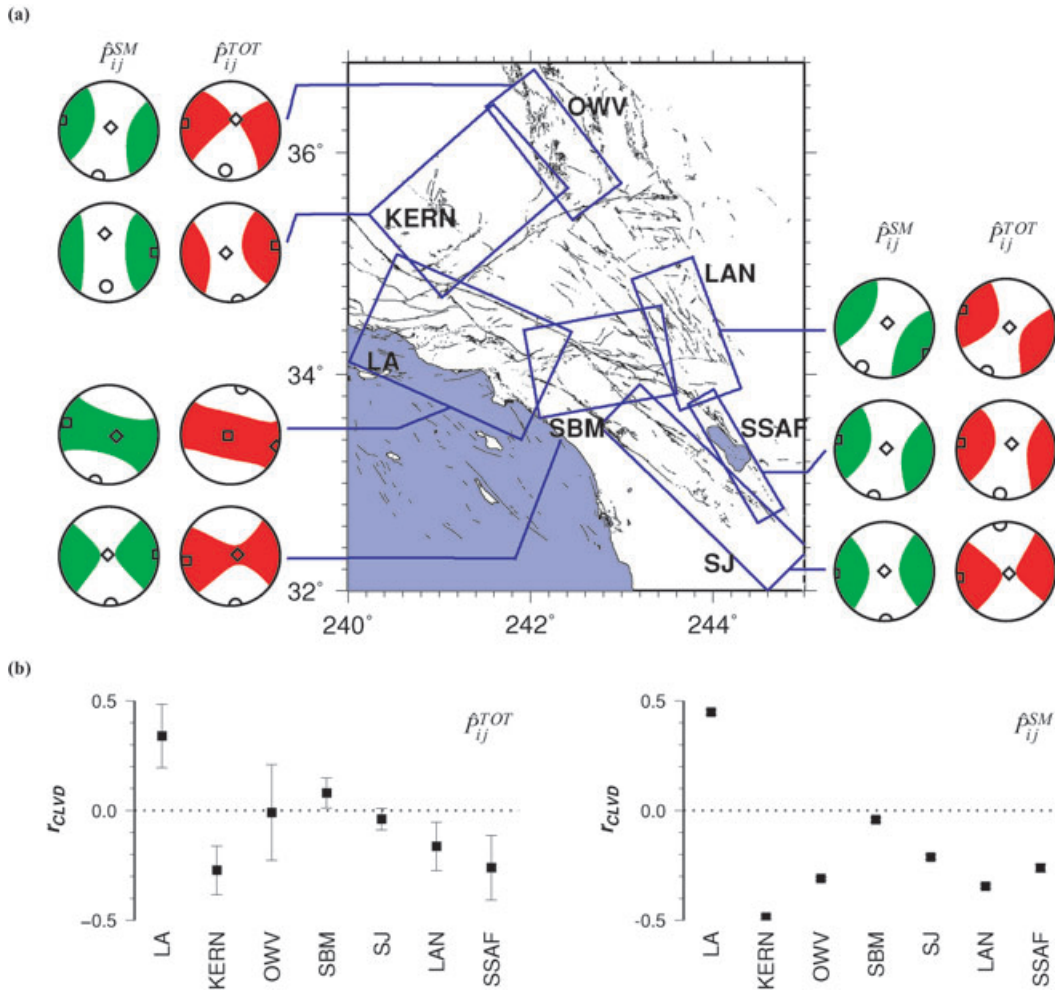


**Figure 5.** (a) Summations of potency tensors and source mechanism tensors for seven tectonically defined regions, using earthquakes in the range  $0 < M_L \leq 5$ . The radii of the beachball plots are equal, such that these represent the normalized tensors,  $\hat{p}_{ij}^{TOT}$  and  $\hat{p}_{ij}^{SM}$  for each bin. *P*-, *B*- and *T*-axis orientations are overlain as in Fig. 2. (b) Values of  $r_{CLVD}$  for the different regions. Error bars show the 95% confidence limits predicted by bootstrap analysis. For the source mechanism summations, these limits are all smaller than the symbol size.

### 3.4 Magnitude bins for tectonic regions

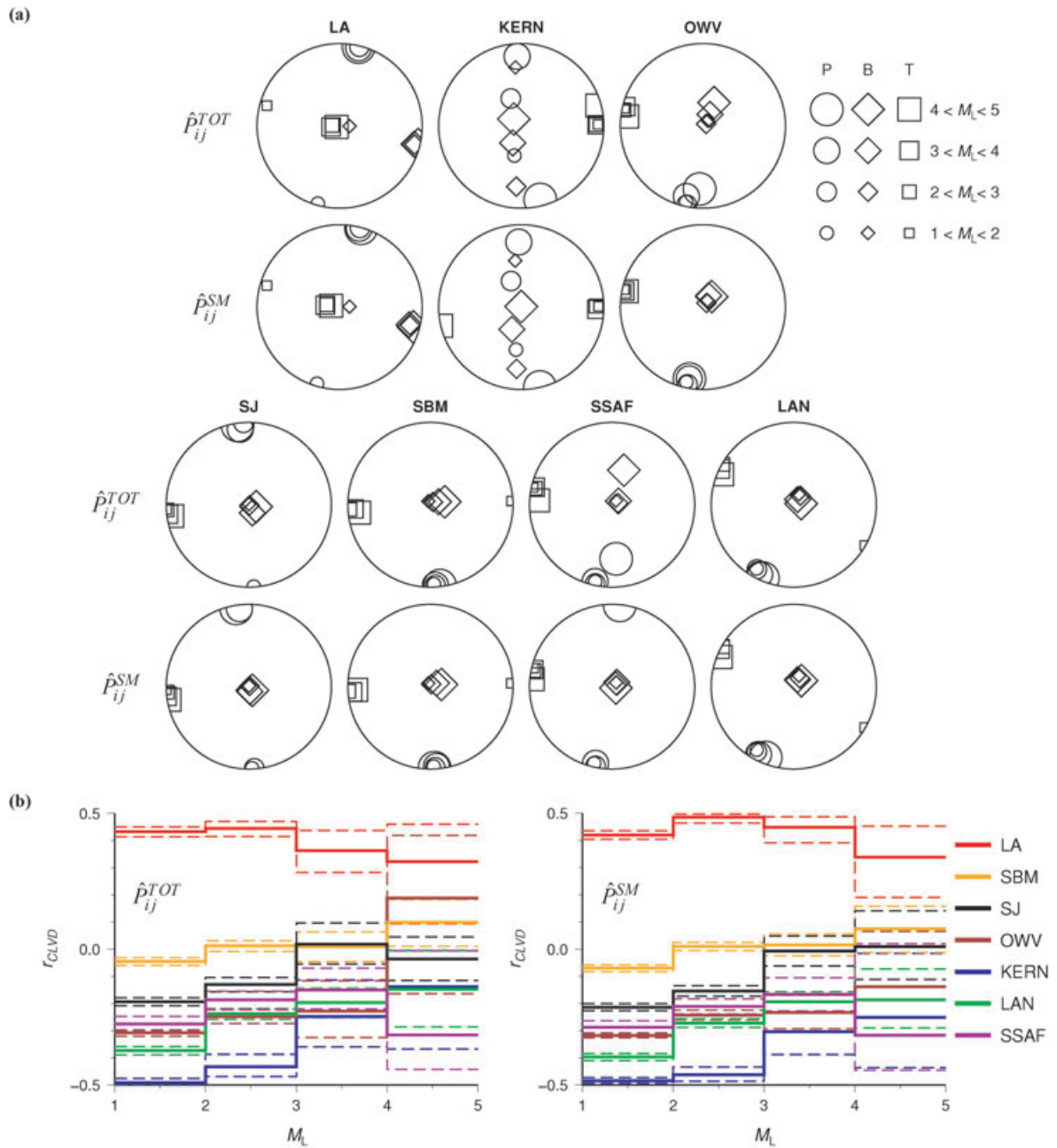
To unite the results for magnitude and regional binning, we further subdivide each of the regions using the four largest magnitude bins. Results for the range  $0 < M_L \leq 1$  are omitted because of strong spatial variations in catalogue completeness at these magnitudes.

Fig. 6 displays results associated with  $\hat{p}_{ij}^{TOT}$  and  $\hat{p}_{ij}^{SM}$  for different magnitude bins in each of the seven regions. To overlay several results we do not plot the beachballs, but the same information is provided in terms of (a) the strain axis orientations using different sized symbols for different magnitude bins and (b) the values for  $r_{CLVD}$ . The results complement those for the magnitude separation of the entire catalogue (Fig. 4), showing that the strain axis orientations in each region are closely aligned over multiple magnitude ranges, whereas the CLVD component tends to become larger for summations over populations of smaller earthquakes. Region KERN appears to show unstable *B*- and *P*-axis orientations, but this can be related to the large negative value of  $r_{CLVD}$ , which means that there is little difference between the size of the intermediate and compressive strains. To define the orientation of a pure CLVD mechanism with  $r_{CLVD} = -0.5$ , only the *T*-axis direction is necessary, which in this case remains stable. A similar effect is shown in

the LA region, where the *P*-axis remains stable whereas the *T*- and *B*-axis orientations switch for the  $1 < M_L \leq 2$ .

### 3.5 Quality-based analysis

We address the effects of variable data quality by repeating the magnitude and regional partitioning for catalogues with different quality restrictions. In the *HASH* algorithm, A, B and C quality mechanisms are defined as those with FPU less than or equal to 25°, 35° and 45°, respectively, where stations used for computation of all mechanisms must have a maximum azimuthal gap less than 90° and maximum takeoff angle gap less than 60°. However, applying only the azimuthal and takeoff angle gap restrictions reduces the number of focal mechanisms to ~24 000 (~15% of the number of data used in this study). We neglect these restrictions in our study and define quality entirely based on FPU. We define five levels of increasingly higher quality by imposing cutoff values for the maximum acceptable FPU: 42°, 35°, 31°, 28° and 24°, chosen to return the best constrained 25, 10, 5, 2.5 and 1% of the data, respectively. The preference of higher quality focal mechanisms leads to biases toward earthquakes of larger magnitude and those



**Figure 6.** (a) Equal area projections showing orientation of the principle strain axes (different shapes) for summed tensors in different magnitude bins (different symbol sizes). (b)  $r_{CLVD}$  over different magnitude ranges for each of the seven regions (different colours). Dashed lines show the 95% confidence intervals for  $r_{CLVD}$  in each of the summations based on a bootstrap analysis.

in well instrumented regions because they are recorded by more seismic stations. Since this study investigates the effect of magnitude and location-based selection upon summed tensors, we can expect these quality-related biases to influence our results. Because of this we do not necessarily interpret the results from higher quality data as showing the true nature of the deformation, but identify the changes in results due to step-by-step increases in quality, using these changes to indicate possible artefacts. To better constrain the effects of earthquake magnitude biases in the summations, we concentrate our analyses for higher quality catalogues on the results for source mechanism summations. We also impose a requirement of

at least 30 events for each summation to retain reasonably robust estimates of average properties.

Fig. 7 shows results for the southern California source mechanism summations of Section 3.2 using magnitude bins with increasingly higher quality restrictions. The results are displayed in terms of (a) the axis orientations and (b)  $r_{CLVD}$  for bins in the largest four magnitude ranges, where colours represent different quality levels. The orientations are most stable for the  $4 < M_L \leq 5$  subset, but in general, orientations for all magnitudes are similar until the highest quality restriction ( $FPU \leq 24^\circ$ ) is applied. Out of the three axes, the *B*-axis and *T*-axis orientations vary more strongly

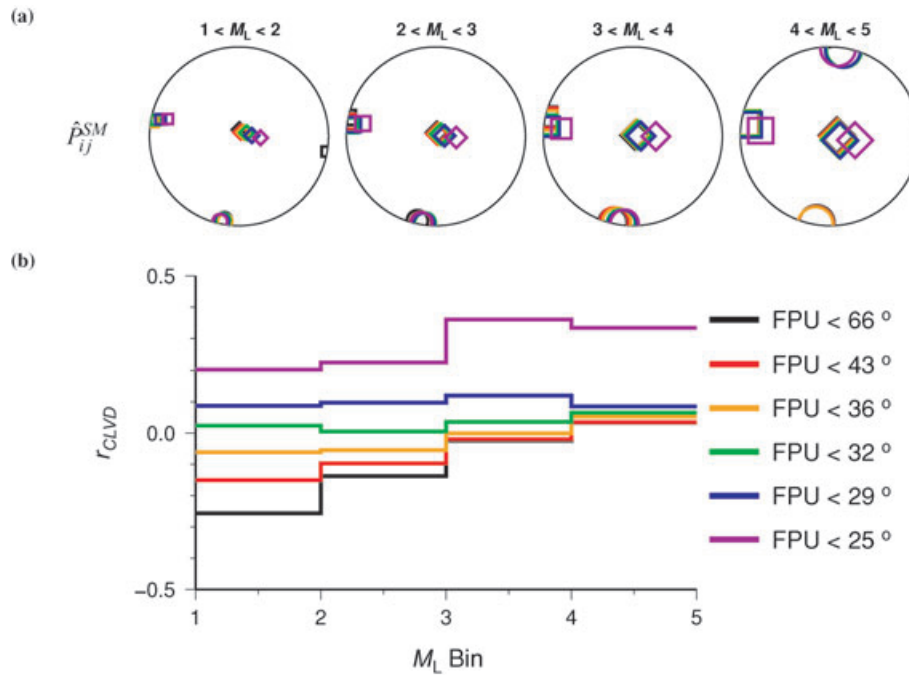


**Figure 7.** (a) Orientations of  $P$  (circle),  $B$  (diamond) and  $T$  (square) axes of  $\hat{P}_{ij}^{SM}$  for the magnitude bins (different stereonets) of the entire catalogue when different quality restrictions (different colours) are imposed on the data. (b)  $r_{CLVD}$  for the source mechanism summations over different magnitude bins for different quality thresholds. Results are only displayed for summations where the number of events is greater than 30.

than the  $P$ -axis, which relates to a CLVD component that becomes more positive with higher quality in Fig. 7(b). The values of  $r_{CLVD}$  show that the correlation between magnitude and negative CLVD component becomes less significant when intermediate quality restrictions are applied, disappearing when  $FPU \leq 31^\circ$  and switching to become strongly positive for higher quality data sets. The results of Section 3.3 indicate that most reverse faulting is concentrated in LA, which is a well instrumented region, implying that earthquakes from this region are preferentially sampled with the higher quality restrictions. It is therefore unclear if the disappearing trend in  $r_{CLVD}$  for intermediate quality restrictions is due to a growing dominance of LA data, or if the correlation between magnitude and CLVD component is an artefact of low quality data. However, given the subsequent results for regions SJ and SSAF where correlations are preserved at higher quality, we favour the former interpretation.

Application of the same quality analysis to the seven tectonic regions reproduces similar results in that the CLVD values are more sensitive than the principle strain axis orientations to data quality. In Fig. 8 we show the values of  $r_{CLVD}$  when these restrictions are applied to four of the regions: LA, SBM, SJ and OWV (LAN and SSAF are not well sampled at lower magnitudes, KERN is not at high magnitudes). The black lines reproduce the results for minimal quality restrictions shown in Fig. 6, whereas coloured lines correspond to the same quality restrictions used in Fig. 7. The quality restrictions have different effects in the different regions, but these are likely to result from the strong sensitivity of the CLVD component to spatial sampling rather than an increased number of low quality data. For the SJ and SBM cases, the CLVD trend is largely preserved for higher quality catalogues, indicating no evidence for an explanation based on catalogue uncertainties. In the OWV case, the CLVD component remains large, but the correlation with magnitude becomes less prominent as quality increases. In the LA case, summations based on higher quality data show a smaller CLVD component for all magnitudes. Combined, these results are

ambiguous in terms of the relationship between the CLVD component and data quality, though there is no clear correlation of our CLVD observations being explained by data uncertainty. It is likely that reverse faulting in the Los Angeles Basin is better sampled than the surrounding strike-slip faulting, and higher quality catalogues are simply reflecting different spatial biases.

### 3.6 Gridded tensor summations for 1 km-scale spatial analysis

#### 3.6.1 Methods

In a second approach to spatial analysis, we investigate source mechanism summations at a 1 km resolution for two regions. The first is the trifurcation region of the San Jacinto fault in the San Jacinto Mountains (TRIF in Fig. 1). We define a  $75 \text{ km} \times 75 \text{ km}$  to encompass the region and compute the summed tensor  $\hat{P}_{ij}^{SM}$  for  $1 \text{ km}^2$  grid cells that contain earthquakes in our catalogue. We choose this region because the relatively dense network coverage has led to a high number ( $N = 12\,708$ ) of data, including a large number of small events and thus wide spatial sampling. The grid cells are defined by choosing the most southwesterly point of the region and denoting boundaries at 1 km intervals to the north and east. We choose 1 km as a scale, since it is larger than 98% of horizontal location errors within the catalogue. The depth extent of each grid cell is set uniformly to 15 km, such that the volume of crust is approximately equal for all cells. The second region is SBM in Fig. 1, which has dimensions  $140 \times 90 \text{ km}$  and is centred over the intersection of the San Jacinto and San Andreas faults in the San Bernardino Mountains. A horizontal grid is defined in the same way as for TRIF, though the grid itself is rotated anti-clockwise by  $10^\circ$  from a north–south, east–west orientation. This second region provides a useful comparison, since it is larger than TRIF and includes

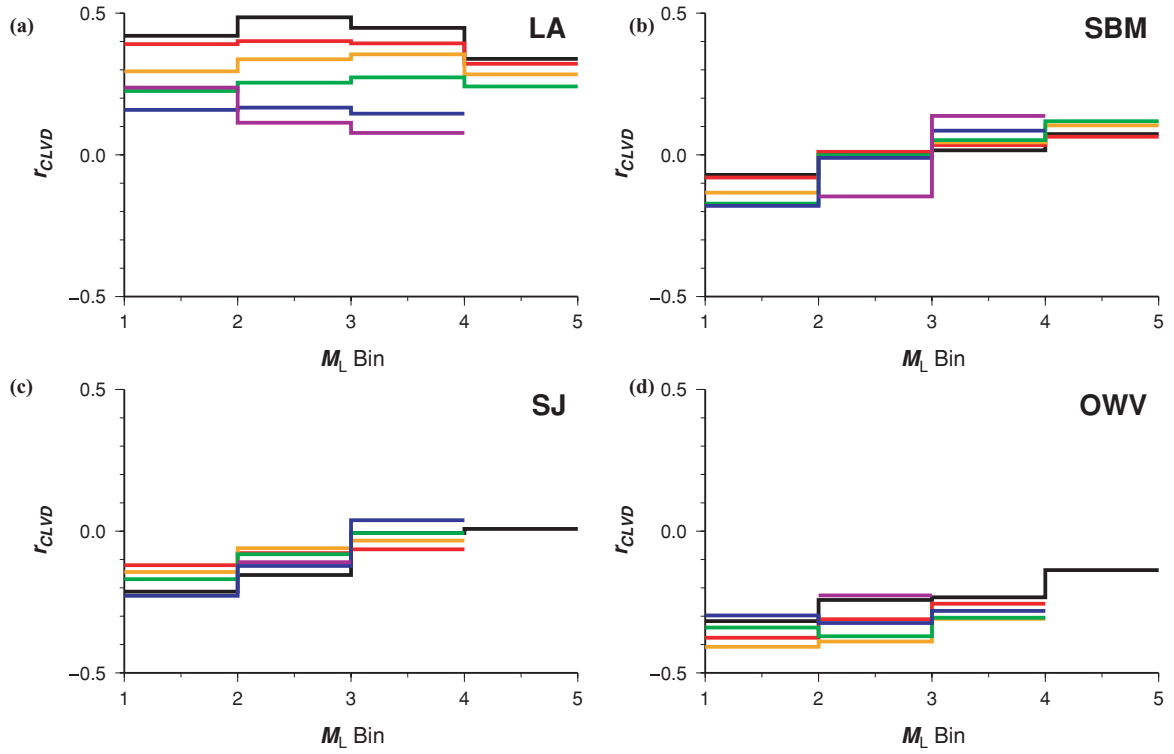


**Figure 8.**  $r_{\text{CLVD}}$  for the normalized summations over different magnitude bins, given different quality thresholds. Line colours are the same as for Fig. 7. The lowest quality threshold (black line) is equivalent to no quality restrictions, as shown in Fig. 6. Results are only displayed where the number of events is greater than 30. (a) Region LA. (b) Region SBM. (c) Region SJ. (d) Region OWV.

data that sample a greater diversity of faulting structures as well as including the 1992 Big Bear aftershock sequence.

We neglect the depth information of earthquakes for both regions to simplify the analysis and retain a reasonable number of events in grid cells. As the regions are both strike-slip dominated regimes, we assume that faults have a greater influence on horizontal variations in the earthquake orientations, and combining the entire range of depths increases the number of data we can use. We relate our results to fault geometries using the map of Jennings (1975).

We allocate earthquakes to each grid cell using two separate techniques. In the first, referred to as a ‘gridded summation’, we compute  $\hat{P}_{ij}^{SM}$  based on earthquakes within the grid cell boundaries. At these scales, the number and quality of data in each grid cell can vary significantly, and we wish to assess the robustness of results by taking this variation into account. We therefore consider a second ‘quality-adaptive summation’ method, where rather than including only the  $N_{\text{cell}}$  earthquakes located within the grid cell, we include the nearest  $N$  events to the centre of the grid cell. We define  $N$  such that  $N \geq N_{\text{cell}}$  and the summed quality,  $\sum_{i=1}^N q_i$ , is greater than 15, where  $q_i$  is given by the *HASH* measure *PROB*. Hence each summation is based on at least 15 tensors. We choose 15 as a cutoff since this leads to most summations being based on  $\sim 30$  events which is a typical number used to validate asymptotic behaviour in statistical studies. The quality adaptive summation cannot be interpreted on its own, since the method has the effect of smoothing out spatial variations in areas of sparse data. This may not represent true variations, but it allows us to understand how much resolution is allowed by the data for a given location and assess the robustness of the gridded summation results.

For these results where we compare large number of tensor summations, it becomes impractical to use the beachball plots to display

summed tensor properties. We therefore describe the orientation of the principle strain axes using the horizontal projection of the  $P$ -axis and a measure of faulting style,  $\gamma_{FS}$ , that quantifies which of the principle strain axes is most vertical. The size of the CLVD component in each grid cell is represented by the value of  $r_{\text{CLVD}}$ .

The dominant faulting style may be described by a function of the vertical components of the three eigenvectors,

$$\gamma_{FS} = \arctan\left(\frac{|e_{33}| - |e_{13}|}{\sqrt{2}|e_{23}|}\right), \quad (10)$$

where  $e_{i3}$  refers to the vertical component of the  $i$ th eigenvector, as defined in Section 3.1. The angle  $\gamma_{FS}$  ranges from  $-90^\circ$  to  $90^\circ$ , and in the case of a DC mechanism it returns the rake angle. If  $\gamma_{FS} = -90^\circ$ ,  $|e_{13}| = 1$  and  $\mathbf{e}_1$  must be vertical so the tensor corresponds to a dominance of normal faulting. If  $\gamma_{FS} = 90^\circ$ ,  $\mathbf{e}_3$  must be vertical and the tensor corresponds to a dominance of reverse faulting. If  $\gamma_{FS} = 0$ , it is either because  $\mathbf{e}_2$  is vertical or because  $\mathbf{e}_1$  and  $\mathbf{e}_3$  have the same plunge, which implies a dominance of strike-slip faulting. Because of the fault plane ambiguity, no distinction can be made about right-lateral versus left-lateral faulting based on this parameter.

### 3.6.2 Results for TRIF

Results for gridded and quality adaptive summations across region TRIF using the entire magnitude range are shown in Fig. 9. Fault traces are shown by light grey lines and the fault trifurcation itself is indicated by a black box in Fig. 9(b). Each grid cell in Fig. 9(a) is coloured according to the value of  $\gamma_{FS}$  (red for dominant reverse faulting, yellow for strike-slip, blue for normal), and in every second grid cell we display the horizontal projection of the  $P$ -axis using

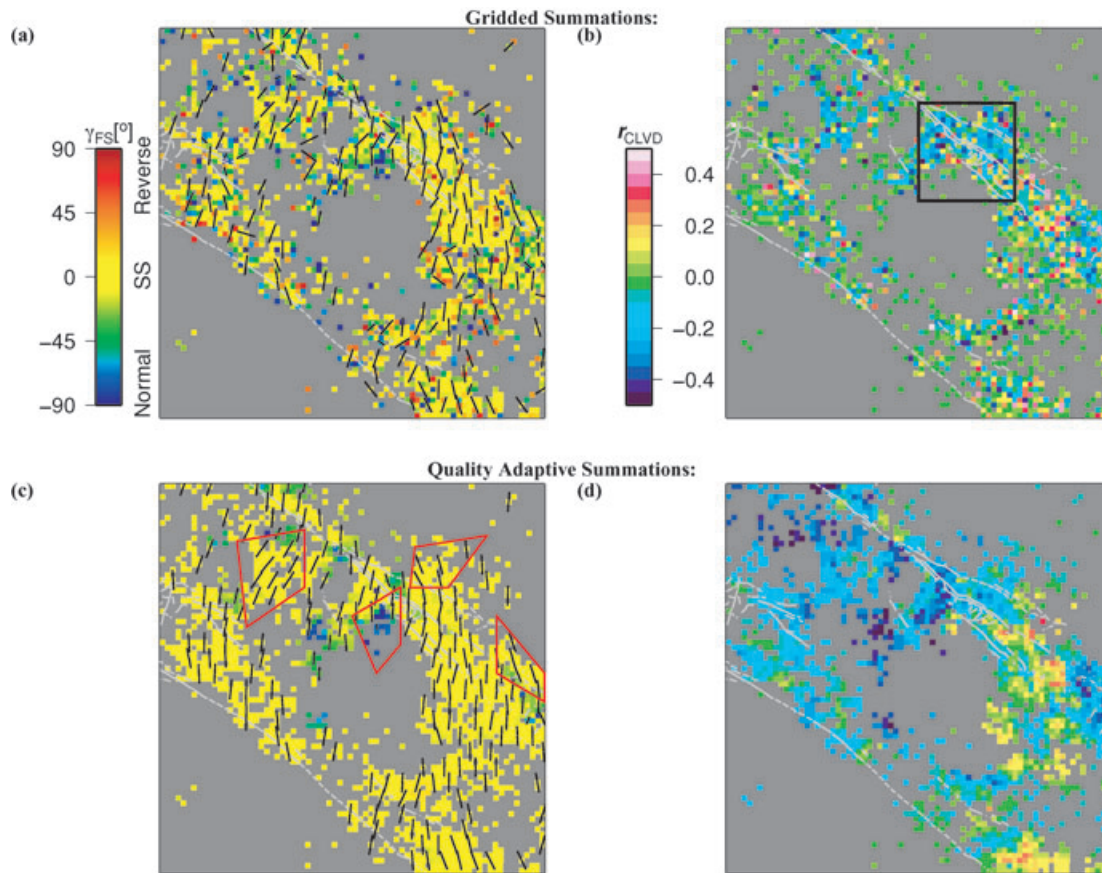


**Figure 9.** Results of gridded tensor summations for region TRIF (see Fig. 1) based on a  $1 \times 1$  km horizontally defined grid, displayed in terms of (a) the dominant faulting style,  $\gamma_{FS}$ , of each grid cell and (b) the value of  $r_{CLVD}$  in those cells with at least three events. The quality-adaptive summation results for the same data are shown in (c) and (d). For the parameter  $\gamma_{FS}$ , red corresponds to dominant reverse faulting, yellow to strike-slip and blue to normal faulting. The black rectangle in (b) indicates the location of the San Jacinto Fault trifurcation referred to in the text. Red polygons in (c) indicate areas where the strain axis orientations of grid cell summed tensors persistently differ from the orientations of the regional summed tensor.

black bars. In Fig. 9(b), we display the associated value of  $r_{CLVD}$  for the summed tensor in grid cells with at least three events, since the distribution of  $r_{CLVD}$  in our random simulations (Appendix D) is the same for  $N \geq 3$ . Corresponding results based on quality-adaptive summations are shown in Figs 9(c) and (d).

The large yellow regions in Figs 9(a) and (c) highlight a dominance of strike-slip faulting ( $\gamma_{FS} \sim 0$ ) over the region, consistent with the overall deformation. We also observe grid cells with dominance of both reverse ( $\gamma_{FS} \sim 90^\circ$ ) and normal faulting ( $\gamma_{FS} \sim -90^\circ$ ), and in Fig. 9(a) these two extremes exist in adjacent grid cells at certain locations. However, the quality-adaptive summations in Fig. 9(c) allow us to show that much of this apparent spatial heterogeneity is not robust given the number and quality of data. Similar heterogeneity in the  $P$ -axis azimuths is strongly reduced by the quality-adaptive summation, such that most variation is within a few degrees of the north–south trend shown by the San Jacinto summed tensor in Fig. 6. Departures from the background strain axes orientation appear to be robust in a number of locations; most notably for an  $\sim 8$  km region to the southwest of the fault trifurcation where we find that normal faulting dominates. This anomaly may relate to the complexity of the nearby trifurcation or to its position within a step-over, though the right-lateral nature of the strike-slip faults would imply compression in such a step-over. We also observe several smaller-scale regions with tendencies toward normal faulting, and five or six regions where the  $P$ -axis azimuth undergoes distinct orientation changes. From visual inspection, many of

the changes in azimuth orientation correspond to nearby changes in the fault geometries, indicating that faults locally exert control over earthquake orientations.

We find an apparent correspondence between regions where the summed tensor axis orientations differ from the background in Figs 9(a) and (c), and locations of non-zero values of  $r_{CLVD}$  in Figs 9(b) and (d). This suggests that the CLVD component becomes more significant in localized regions where the faulting style deviates from the regionally dominant sense of deformation.

### 3.6.3 Results for TRIF magnitude bins

Figs 10 and 11 exhibit results of both gridded summations and quality-adaptive summations for magnitude subsets of region TRIF in terms of  $\gamma_{FS}$  and  $r_{CLVD}$ . In Fig. 10 the results are presented for grid cells that contain at least one event, whereas in Fig. 11 the results are only displayed for grid cells with at least three events. The lack of data in the upper magnitude ranges means that we only display results for  $0 < M_L \leq 4$  in Fig. 10 and  $0 < M_L \leq 3$  in Fig. 11. Beachball plots showing the results of  $\hat{P}_{ij}^{SM}$  and the associated values of  $r_{CLVD}$  for each magnitude range over the entire region are also displayed in Fig. 10.

We see no clear differences between spatial patterns of the strain axis orientations for different magnitude bins, such that the robust non-strike-slip features observed in Fig. 9 are found for all

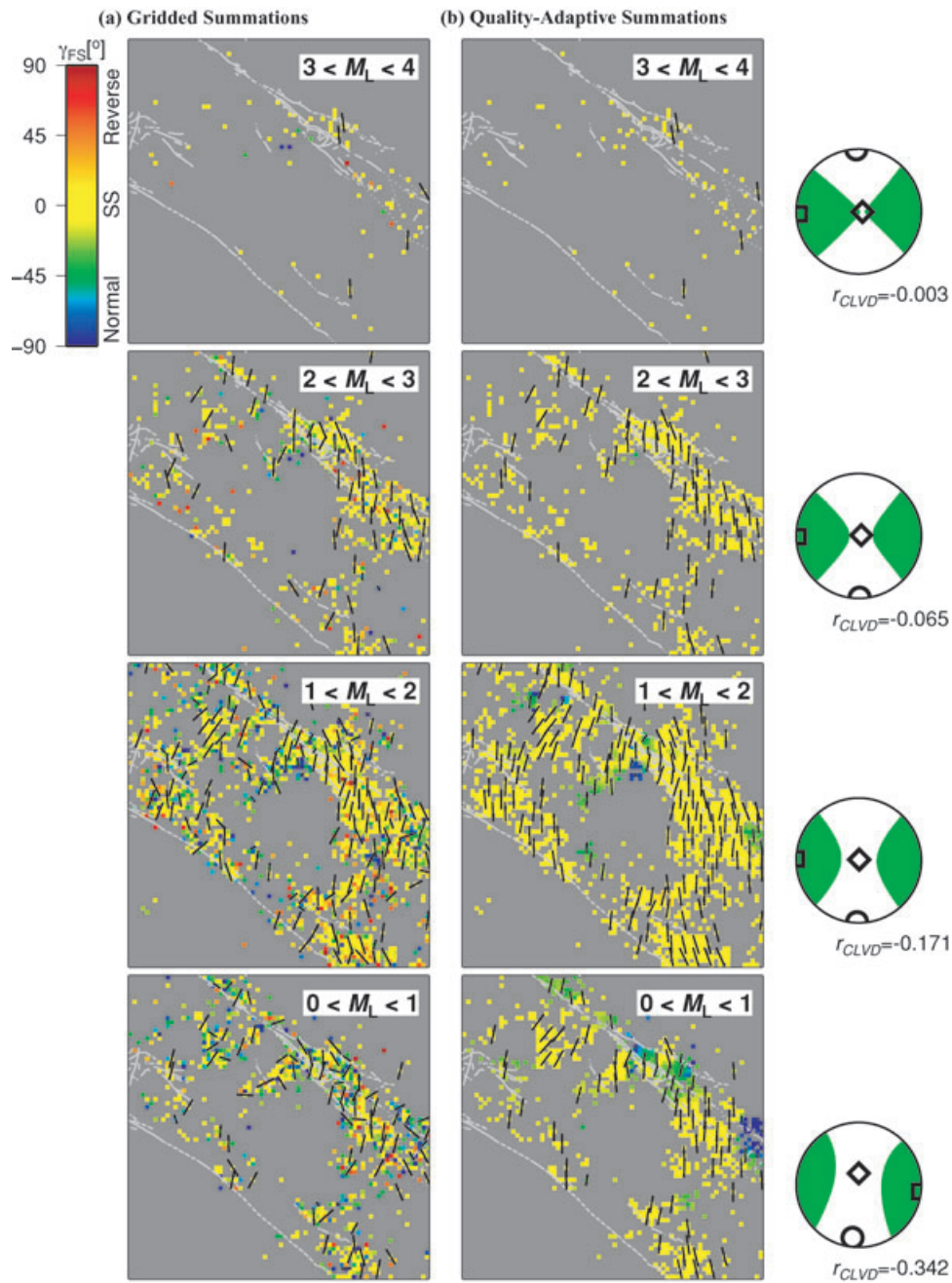


**Figure 10.** The (a) gridded summation and (b) quality adaptive summation results of  $P_{ij}^{SM}$  for region TRIF over four magnitude bins displayed in terms of dominant fault style (colours) and  $P$ -axis azimuths (bars). Source mechanism summations for all earthquakes in the region are shown by beachball plots and  $r_{CLVD}$  values to the right.

magnitude ranges when data exist in those locations. This implies that persistent length-scales control earthquake behaviour regardless of magnitude over a range of at least four magnitude units. Most of these persistent length-scales are robust according to the quality-adaptive summation except in the range  $3 < M_L \leq 4$ , where the number of data is not sufficient to robustly image any local features shown by the gridded summation. However, the persistence of these features at multiple magnitude levels indicates that they are not a result of random noise, and this highlights the problem of small data sets when studies are restricted to larger earthquakes. The major difference between data from different magnitude ranges is shown to be the spatial coverage, and this feature affects which faulting

structures are sampled by the regional summations in previous sections. Events in all magnitude ranges appear most likely to occur close to the dominating fault structures, but the greater likelihood of imaging off fault structures is provided by earthquakes in the  $1 < M_L \leq 2$  range.

In Fig. 11, we observe that the spatial variation in  $r_{CLVD}$  of Fig. 9 is broadly reproduced at all three magnitude levels. The histograms plotted in Fig. 11(a) show the distribution of  $r_{CLVD}$  across the grid cells for each magnitude range. The distributions are distinctly skewed to the left, reflecting the negative values for  $r_{CLVD}$  of the regionally summed tensors of Fig. 10. However, noticeable peaks at  $r_{CLVD} = 0$  show that for a large proportion of the grid cells, the

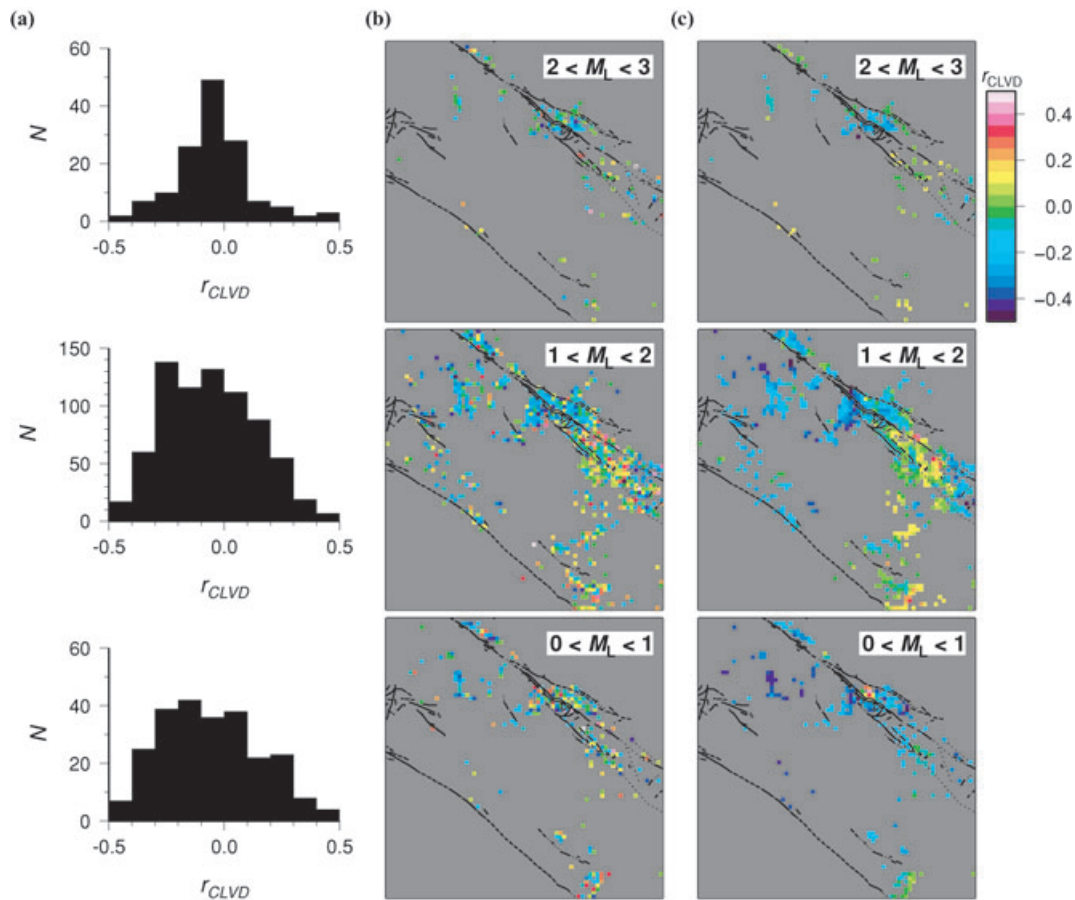


**Figure 11.** Values of  $r_{\text{CLVD}}$  computed from those gridded summations used for Fig. 10 that include at least three events. (a) Histograms showing  $r_{\text{CLVD}}$  distributions for the grids ( $N$  is the number of grid cells), (b) gridded summation results and (c) quality adaptive summation results for three magnitude bins.

source mechanism summation is close to a DC. The histograms demonstrate narrower distributions of  $r_{\text{CLVD}}$  for higher magnitude, correlating with the smaller values of  $r_{\text{CLVD}}$  given in Fig. 10. This may be explained by decreased sampling of more complex structures with populations of larger earthquakes. However, the number of data in grid cells is relatively small and the histograms may alternatively reflect increased uncertainties in focal mechanism data for lower magnitude populations.

### 3.6.4 Results for SBM magnitude bins

In the case of region SBM, the network does not provide enough spatial coverage for us to analyse the lowest magnitude range and we therefore show only results for  $1 < M_L \leq 4$  (Figs 12 and 13). The dominant potency release for region SBM (Fig. 5) has a near vertical  $B$ -axis (i.e. strike-slip faulting) and north–south  $P$ -axis orientations corresponding to the strike of the San Andreas Fault in the region, despite a lack of seismicity there. This is reflected in Fig. 12 by the large yellow coloured regions and generally north–south trending azimuth bars. Most of the region conforms to this pattern, showing that the SBM summed tensors in Fig. 5 reflect spatial coverage that extends beyond that of the aftershocks of the Big Bear earthquake. As observed for region TRIF, we find that a high degree of spatial heterogeneity indicated by the gridded summations is greatly reduced by the quality-adaptive summations. However, we identify three robust regions of non-strike-slip faulting with fixed lengths of  $\sim 20$ – $50$  km (shown by red boxes in Fig. 12a) which correspond to

fault kinks or fault intersections. As well as changes in fault style, the  $P$ -axis azimuths highlight distinct regions of changing fault orientations, which are in most cases in agreement to the fault traces displayed on the map.

Fig. 13 shows that regions of non-strike-slip faulting correspond to regions of high CLVD component, as observed for the TRIF region (Fig. 11). Histograms of the  $r_{\text{CLVD}}$  values for grid cells also show strong peaks close to  $r_{\text{CLVD}} = 0$  for all magnitude ranges, and broadening distributions for lower magnitude ranges. The trend for an increasingly negative CLVD component in Figs 6(b) and 8(b) in lower magnitude data sets is reflected by the broadening of histograms in Fig. 13 and a slight increase in asymmetry of the distribution.

## 4 DISCUSSION

For nearly all spatial scales and regions considered, we find that the orientations of the principle strain axes for summed potency tensors are independent of the magnitude range considered, regardless of the dominant faulting style and temporal nature of seismicity. This observation agrees with the results for other regions of Fischer & Jordan (1991), Amelung & King (1997), and Sheridan (1997). Unlike Amelung & King (1997) we do not consider this to be evidence of a self-similar deformation process, but rather a magnitude-independent response of earthquakes to dominant types of deformation and associated length-scales that are stationary over the time period considered.

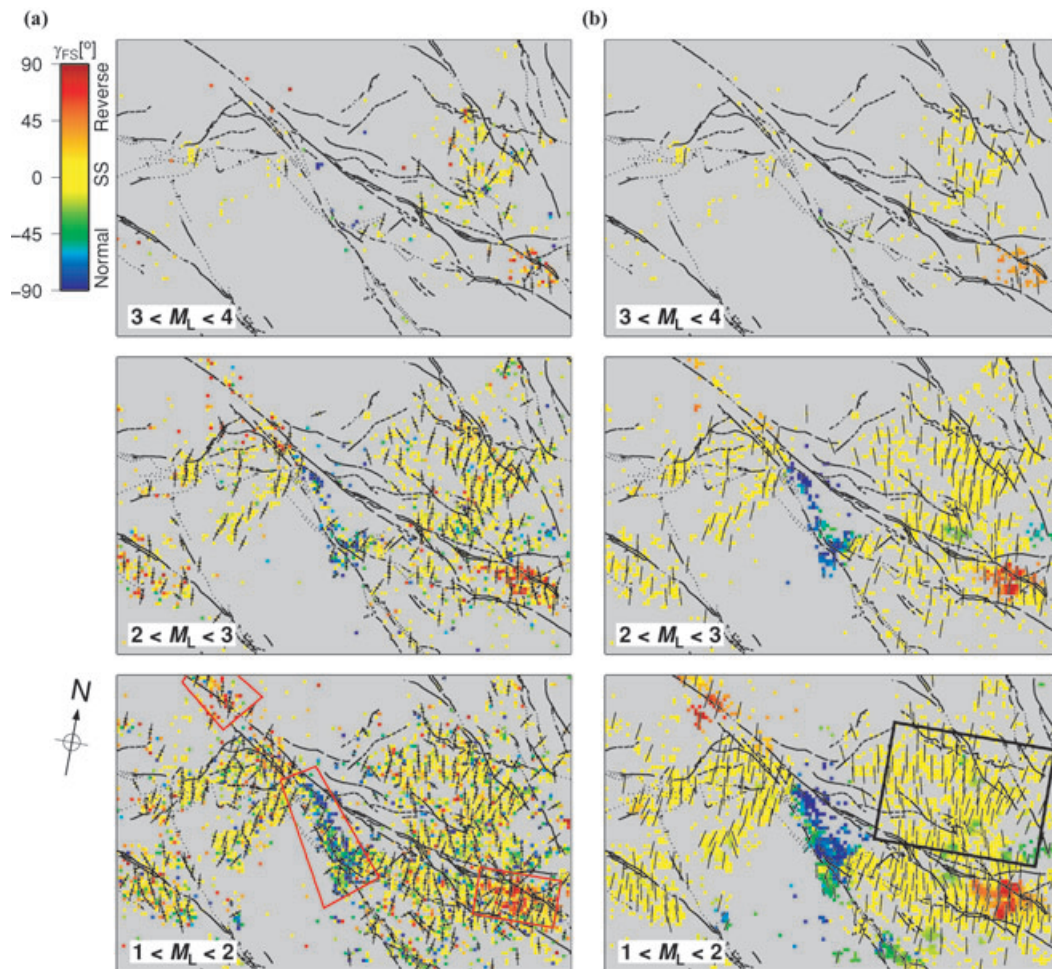


**Figure 12.** The (a) gridded summation and (b) quality adaptive summation results of  $P_{ij}^{SM}$  for region SBM over the middle three magnitude bins, displayed in terms of dominant fault style (colours) and  $P$ -axis azimuths (bars). The black rectangle in the  $1 < M_L \leq 2$  range of (b) highlights the region dominated by aftershocks of the 1992 Big Bear earthquake. The red rectangles in the  $1 < M_L \leq 2$  range of (a) highlight the robust persistent features of non-strike-slip dominated faulting.

At the largest scale ( $\sim 700$  km), the alignment of earthquake orientations with plate motion directions suggests that the length-scales of plate tectonics influence the dominant earthquake behaviour. At the scale of our seven tectonic regions ( $\sim 50$ – $250$  km), the orientations of summed tensors are more consistent with the dominant strike of faults in the region than with the plate motion direction, suggesting that the relevant length-scales are those of the largest faults. At the smallest scale considered, our 1 km spatial grid analyses indicate that most of the potency release within a region is consistent with the largest faults, although there are clear departures over smaller persistent length-scales with a range of sizes ( $\sim 5$ – $50$  km). We may physically interpret the largest length-scale as the overriding response of the whole region to plate loading, the second-order length-scales as the large fault-zones characterized by persistent dominating fault orientations (e.g. Becker *et al.* 2005), and the third-order length-scales as the geometrical complexities within those fault zones.

When taking the CLVD components into account, we find clear differences between summed tensors for different magnitude and spatial bins. These differences indicate a lack of self-similarity in the faulting structures/length-scales that influence seismic behaviour. Out of the seven tectonic regions, the CLVD components are highest in regions KERN and LA, where the principle strain

axis orientations are most different from those of the southern California summations. These regions have a significant component of normal and reverse faulting, respectively, and the CLVD components indicate that these faulting styles mix with the strike-slip style that dominates the southern California region. We therefore suggest that the CLVD components represent heterogeneity that is a function of the difference between the orientation of dominant fault structures and the orientation of the overlying plate motion directions. The same interpretation may be applied to observations of CLVD components at smaller scales.

Within regions TRIF and SBM, most of the grid cells have small CLVD components and axis orientations consistent with the region's summed tensor. Areas where the CLVD component is large are localized and correspond to locations where the axis orientations are different. This indicates a mixing of earthquake slip corresponding to local faulting structures with slip corresponding to the dominant orientation of the fault zone, plate boundary or both. Such mixing may relate to complexities in the stress field generated by geometrical features of the fault zone. At the scale of these geometrical complexities, which we interpret as third-order length scales, the nature of summed tensors are therefore more heterogeneous as they include responses to the plate boundary scale stress, the dominant fault zone orientation as well as very local orientations of stress and

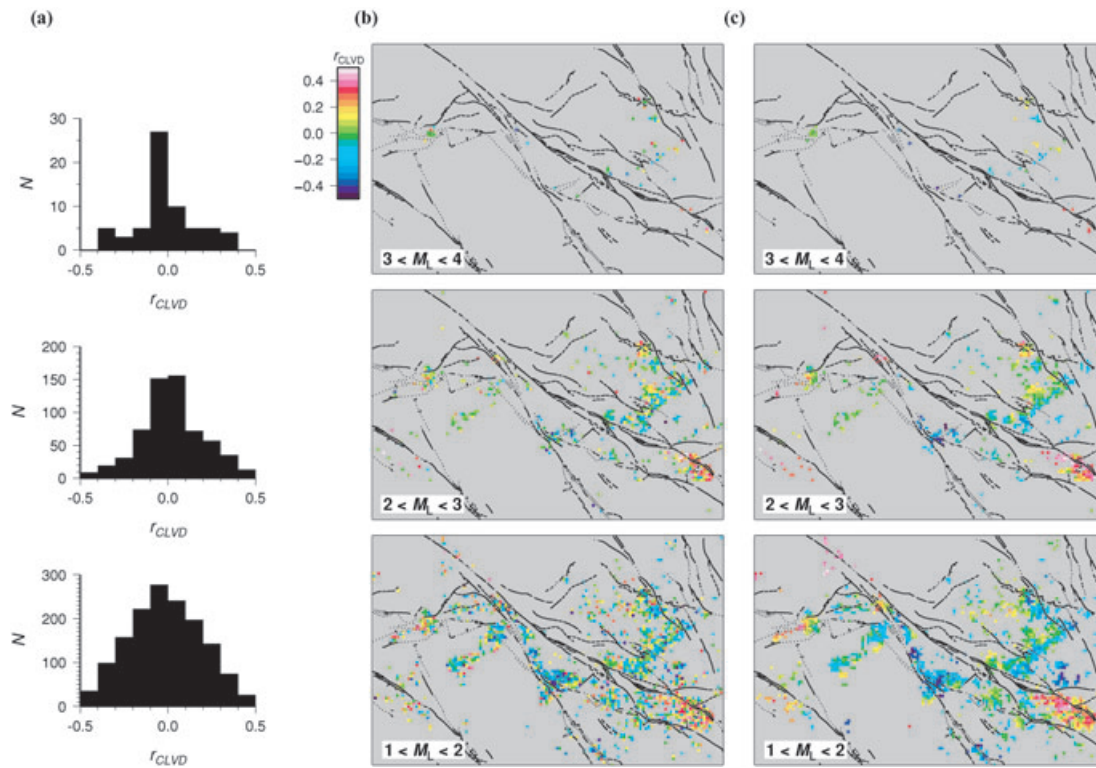


**Figure 13.** Values of  $r_{CLVD}$  are computed from those gridded summations used for Fig. 12 that include at least three events. (a) Histograms of  $r_{CLVD}$  for the number of grid cells in the gridded summation, (b) gridded summation results and (c) quality adaptive summation results for three magnitude bins.

faulting. Since there is some non-uniqueness in the heterogeneity of faulting that may generate a CLVD component, it is unclear from the analysis whether this heterogeneity reflects individual faults that are rougher than the dominant faults, or whether deformation is accommodated by a set of faults with highly varied orientations. However, accounting for a number of small length-scales associated with heterogeneity of strain axis orientations can explain the CLVD components associated with large fault zones and hence the geometrical differences between them.

The analysis of regions TRIF and SBM also allows us to provide an explanation for the apparent magnitude-dependence of CLVD components. The results for specific grid cell localities over different magnitude ranges do not show much variation, but the number of grid cells containing earthquakes, and hence amount of spatial sampling in the analysis, is much larger for smaller earthquakes. As noted above, most grid cells have a small CLVD component, whereas high CLVD components are concentrated in small localized areas of heterogeneity. As smaller magnitude ranges are considered, the spatial sampling increases to include more of these areas, increasing the CLVD component for the overall summed tensor. We may ask whether these localities are not represented in populations of large earthquakes because there are not enough data or because there are physical limitations to the occurrence of large events there. A physical limitation is plausible since larger and smoother potential rupture surfaces will aid the chances of propagation over large distances to generate larger magnitude earthquakes. If we consider the faulting structures of the localities with enhanced heterogeneities to be immature relative to the larger fault zones, this ties together with the interpretation of Ben-Zion & Sammis (2003) that faults evolve from complex to homogeneous structures.

However, further investigation of this point is hindered by the lack of seismicity on the San Andreas Fault which is the region's most mature fault. The focal mechanism analysis of Hardebeck (2006) found that within the data uncertainty, earthquakes generally behave homogeneously over  $\sim 10$  km scales. Our findings support this observation, since most small earthquakes occur in regions of relative homogeneity. We further find that the level and nature of heterogeneity is not always the same, and heterogeneous behaviour can also be localized at a  $\sim 10$  km scale, though a range of scales are observed. These heterogeneous regions are better sampled by smaller earthquakes.

As highlighted by the study of Hardebeck (2006), there can be considerable ambiguity between true earthquake heterogeneity and uncertainty within the data. Our analysis of successively higher quality catalogues shows that differences between regional CLVD components are robust, and artefacts due to low quality data do not explain our observations. However, we also found that values of  $r_{CLVD}$  are more sensitive to data quality than the orientations of the principle strain axes, implying that the CLVD component is the least well constrained component of the summed tensors. This may be explained in view of our interpretations that regional CLVD components are generated by small localized structures within the regions. Focal mechanism quality is largely dependent on the station distribution with respect to the earthquake location (Kilb & Hardebeck 2006), and hence this strong spatial aspect will affect how many of the CLVD contributing localities are sampled by data, given a certain quality cutoff. The quality dependence of the CLVD component therefore supports our interpretations of spatial variation in the heterogeneity of structures. Analysis of likely biases that considers the exact distribution of the employed seismic stations

would provide a more complete understanding of the effects of data quality.

Our results and interpretations have implications for the study of regional strain partitioning, scale-independent aspects of deformation and stress inversions. Our analyses suggest that over ~20 year time periods in a complex plate boundary region such as southern California, the tectonic strain is not partitioned into distinct regions of pure strike-slip, normal and reverse faulting mechanisms. Instead, the deformation is partitioned into regions of relative homogeneity, governed by the largest nearby fault structure, and regions of relative heterogeneity, where the dominant faulting style mixes with local complexities. Our results from various spatial scales suggest that the heterogeneous regions are often confined to small scale faulting structures, whereas the overall deformation of a plate boundary can be understood to first order in terms of a combination of the relatively homogeneous large-scale (~ 50–250 km) fault zones.

The lack of self-similarity observed for different scales and different faulting structures indicates that several specific length-scales are important to how earthquake populations behave. The association of earthquake deformation with scale-invariance is often based on the observation of many power-law distributions in earthquake data (e.g. Turcotte 1997, chapter 4). However, power-law distributions may be produced on planar structures (e.g. Hillers *et al.* 2007), and can also reflect mixing of many populations influenced by a wide range of length-scales (e.g. Ben-Zion 2008), as we infer for our results. The other end of the spectrum is a system for which there is one characteristic dominant scale. The interaction of several different length-scales shows that this description also cannot be used to explain our regional results. Although the large-scale dynamics of the entire system may be captured by taking into account the large faults and the overriding stress field, accounting for the differences between those faults requires taking into account heterogeneities associated with many smaller length-scales that have a wide range of sizes.

Tectonic stress is typically calculated by inversion of focal mechanism data, where focal mechanisms are used as a proxy for fault slip direction (e.g. Angelier *et al.* 1982; Michael 1987). These inversion methods are based on the assumption that the stress is homogeneous for the population of earthquakes to which the inversion is applied. It is therefore important to understand the spatial variations in earthquake behaviour to define suitable spatial bins for the inversion process. Our inference is that the large-scale fault zones control the dominant behaviour of earthquakes across southern California. This may explain how fundamental characteristics of the stress field can fit GPS observations using a fault-defined block model, as done by Becker *et al.* (2005). Fitting the smaller scale variations of stress requires identification of the second and third-order structures interpreted in this study. An approach using appropriate spatial bins based on cluster analyses of the earthquake locations, such as that of Hardebeck & Michael (2004), may be well suited to this goal.

## ACKNOWLEDGMENTS

We thank Jeanne Hardebeck for generating the *HASH* catalogue of focal mechanisms used in this work and Matthias Holschneider for helpful discussions. We are also grateful to the editor, Frank Krueger, and two anonymous reviewers for their comments. This research was supported by the Southern California Earthquake Center (based on NSF Cooperative Agreement EAR-0106924 and USGS Cooperative Agreement 02HQAG0008). The SCEC contribution number for this paper is 1161. All figures were generated using GMT (Wessel & Smith 1998).

## REFERENCES

- Aki, K. & Richards, P.G., 2002. *Quantitative Seismology*, 2nd edn, University Science Books, Sausalito, California, USA.
- Amelung, F. & King, G., 1997. Large-scale tectonic deformation inferred from small earthquakes, *Nature*, **386**, 702–705.
- Ampuero, J.-P. & Dahlen, F.A., 2005. Ambiguity of the moment tensor, *Bull. seism. Soc. Am.*, **95**(2), 390–400.
- Angelier, J., Tarantola, A., Manoussis, S. & Valette, B., 1982. Inversion of field data in fault tectonics to obtain the regional Stress. Part 1. Single phase fault populations: a new method of computing the stress tensor, *Geophys. J. R. astr. Soc.*, **69**, 607–621.
- Becker, T.W., Hardebeck, J.L. & Anderson, G., 2005. Constraints on fault slip rates of the southern California Plate boundary from GPS velocity and stress inversions, *Geophys. J. Int.*, **160**, 634–650.
- Ben-Zion, Y., 1989. The response of two joined quarter spaces to SH line sources located at the material discontinuity interface, *Geophys. J. Int.*, **98**(2), 213–222.
- Ben-Zion, Y., 2001. A note on quantification of the earthquake source, *Seism. Res. Lett.*, **72**, 151–152.
- Ben-Zion, Y., 2003. Key formulas in earthquake seismology, in *International Handbook of Earthquake and Engineering Seismology*, eds Lee, W.H.K., Kanamori, H., Jennings, P.C. & Kisslinger, C., pp. 1857–1875, Academic Press, Boston, MA, USA.
- Ben-Zion, Y., 2008. Collective behavior of earthquakes and faults: continuum-discrete transitions, progressive evolutionary changes and different dynamic regimes, *Rev. Geophys.*, **46**, RG4006.
- Ben-Zion, Y. & Sammis, C.G., 2003. Characterization of fault zones, *Pure appl. Geophys.*, **160**, 677–715.
- Ben-Zion, Y. & Zhu, L., 2002. Potency-magnitude scaling relations for southern California earthquakes with  $1.0 < M_L < 7.0$ , *Geophys. J. Int.*, **148**, F1–F5.
- DeMets, C., Gordon, R.G., Argus, D.F. & Stein, S., 1994. Effect of recent revisions to the geomagnetic reversal time scale on estimates of current plate motions, *Geophys. Res. Lett.*, **21**(20), 2191–2194.
- Eshelby, J.D., 1957. The determination of the elastic field of an ellipsoidal inclusion, and related problems, *Proc. Roy. Soc. Lond.*, **241**(1226), 376–396.
- Fehler, M., House, L. & Kaieda, H., 1987. Determining planes along which earthquakes occur: method of application to earthquakes accompanying hydraulic fracturing, *J. geophys. Res.*, **92**, 9407–9414.
- Fischer, K.M. & Jordan, T.H., 1991. Seismic strain rate and deep slab deformation in Tonga, *J. geophys. Res.*, **96**, 14 429–14 444.
- Frolich, C. & Davis, S.D., 1999. How well constrained are well-constrained *T*, *B* and *P* axes in moment tensor catalogs?, *J. geophys. Res.*, **104**, 4901–4910.
- Giardini, D., 1984. Systematic analysis of deep seismicity: 200 centroid-moment tensor solutions for earthquakes between 1977 and 1980, *Geophys. J. R. astr. Soc.*, **77**(3), 883–914.
- Hardebeck, J.L., 2006. Homogeneity of small-scale earthquake faulting, stress and fault strength, *Bull. seism. Soc. Am.*, **96**(5), 1675–1688.
- Hardebeck, J.L. & Michael, A.J., 2004. Stress orientations at intermediate angles to the San Andreas fault, California, *J. geophys. Res.*, **109**(B11303), doi: 10.1029/2004JB003239.
- Hardebeck, J.L. & Shearer, P.M., 2002. A new method for determining first-motion focal mechanisms, *Bull. seism. Soc. Am.*, **92**, 2264–2276.
- Hardebeck, J.L. & Shearer, P.M., 2003. Using S/P amplitude ratios to constrain the focal mechanisms of small earthquakes, *Bull. seism. Soc. Am.*, **93**, 2434–2444.
- Hardebeck, J.L., Shearer, P.M. & Hauksson, E., 2005. A new earthquake focal mechanism catalog for southern California, in *2005 SCEC Annual Meeting Abstracts*, p. 130, Southern California Earthquake Center, available at <http://www.data.scec.org/research/altcatalogs.html>, July 2008.
- Heaton, T.H. & Heaton, R.E., 1989. Static deformations from point sources and force couples located in welded elastic Poissonian half-spaces: implications for seismic moment tensors, *Bull. seism. Soc. Am.*, **79**(3), 813–841.

- Hillers, G., Mai, P.M., Ben-Zion, Y. & Ampuero, J.-P., 2007. Statistical properties of seismicity of fault zones at different evolutionary stages, *Geophys. J. Int.*, **169**, 515–533.
- Holschneider, M. & Ben-Zion, Y., 2006. Bayesian estimation of faults geometry based on seismic catalog data, *EOS Trans. Am. Geophys. Union, Fall Meet. Suppl.*, **87**(52), Fall Meet. Suppl., Abstract S43D-01.
- Jennings, C.W., 1975. *Fault map of California with locations of volcanoes, thermal springs, and thermal wells*, No. 1 in Geologic Data Map, California Division of Mines and Geology, Sacramento, California, USA.
- Jost, M.L. & Hermann, R.B., 1989. A student's guide to and review of moment tensors, *Seis. Res. Lett.*, **69**, 37–57.
- Julian, B.R., Miller, A.D. & Foulger, G.R., 1998. Non-double-couple earthquakes 1. Theory, *Rev. Geophys.*, **36**, 525–550.
- Kagan, Y.Y., 1982. Stochastic model of earthquake fault geometry, *Geophys. J. R. astr. Soc.*, **71**, 659–691.
- Kagan, Y.Y., 1990. Random stress and earthquake statistics: spatial dependence, *Geophys. J. Int.*, **102**, 573–583.
- Kagan, Y.Y., 1991. 3-D rotation of double-couple earthquake sources, *Geophys. J. Int.*, **106**, 709–716.
- Kagan, Y.Y., 2005. Double-couple earthquake focal mechanism: random rotation and display, *Geophys. J. Int.*, **163**, 1065–1072.
- Kagan, Y.Y., 2009. On geometric complexity of earthquake focal zone and fault system: a statistical study, *Phys. Earth planet. Inter.*, doi: 10.1016/j.pepi.2009.01.006.
- Kagan, Y.Y. & Knopoff, L., 1980. Spatial distribution of earthquakes: the two-point correlation function, *Geophys. J. Int.*, **62**(2), 303–320.
- Kagan, Y.Y. & Knopoff, L., 1985. The first-order statistical moment of the seismic moment tensor, *Geophys. J. R. astr. Soc.*, **81**, 429–444.
- Kilb, D. & Hardebeck, J.L., 2006. Fault parameter constraints using relocated earthquakes: a validation of first-motion focal-mechanism data, *Bull. seism. Soc. Am.*, **96**, 1140–1158.
- King, G.C.P., 1983. The accommodation of large strains in the upper lithosphere of the Earth and other solids by self-similar fault systems: the geometrical origin of  $b$ -value, *Pure appl. Geophys.*, **121**, 761–814.
- Knopoff, L. & Randall, M.J., 1970. The compensated linear vector dipole: a possible mechanism for deep earthquakes, *J. geophys. Res.*, **75**, 4957–4963.
- Kostrov, B.V., 1974. Seismic moment and energy of earthquakes and seismic flow of rock, *Phys. Solid Earth*, **1**, 23–40.
- Kuipers, J., 2002. *Quaternions and Rotations: a Primer with Applications to Orbits, Aerospace, and Virtual Reality*, Princeton University Press, Princeton, NJ, USA.
- Libicki, E. & Ben-Zion, Y., 2005. Stochastic branching models of fault surfaces and estimated fractal dimensions, *Pure appl. Geophys.*, **162**(6–7).
- Michael, A.J., 1987. Use of focal mechanisms to determine stress; a control study, *J. geophys. Res.*, **92**, 357–368.
- Nicholson, T., Sambridge, M. & Gudmundsson, Ó., 2000. On entropy and clustering in earthquake hypocentre distributions, *Geophys. J. Int.*, **142**, 37–51.
- Press, W.H., Teukolsky, S.A., Vetterling, W.H. & Flannery, B.P., 1992. *Numerical Recipes in C*, 2nd edn, Cambridge University Press, New York, USA.
- Reid, H.F., 1910. The mechanics of the earthquake, in *The California Earthquake of April 18, 1906*, Vol. 2, Carnegie Institute, Washington, DC, USA.
- Rice, J.R., 1980. The mechanics of earthquake rupture, in *Physics of the Earth's Interior*, eds Dziewonski, A.M. & Boschi, E., pp. 555–649, Italian Physical Society/North Holland, Amsterdam.
- Riedesel, M. & Jordan, T.H., 1989. Display and assessment of seismic moment tensors, *Bull. seism. Soc. Am.*, **79**(1), 85–100.
- Sagy, A., Brodsky, E.E. & Axen, G.J., 2007. Evolution of fault-surface roughness with slip, *Geology*, **35**, 283–286.
- Sheridan, J., 1997. Secondary Deformation near Strike-Slip Faults, Southern California: Seismic and Structural Studies, *PhD thesis*, University of Oregon, Eugene, Oregon, USA.
- Sipkin, S.A. & Silver, P.G., 2003. Characterization of the time-dependent strain field at seismogenic depths using first-motion focal mechanisms: observations of large-scale decadal variations in stress along the San Andreas Fault system, *J. geophys. Res.*, **108**, B7, 2339–2352, doi:10.1029/2002JB002064.
- Stein, S. & Wysession, M., 2003. *An Introduction to Seismology, Earthquakes, and Earth Structure*, 1st edn, Blackwell Publishing, Oxford.
- Stirling, M.W., Wesnousky, S.G. & Shimazaki, K., 1996. Fault trace complexity, cumulative slip, and the shape of the magnitude–frequency distribution for strike-slip faults: a global survey, *Geophys. J. Int.*, **124**(3), 833–868.
- Thurber, C., 1983. Earthquake locations and three-dimensional crustal structure in the Coyote Lake area, central California., *J. geophys. Res.*, **88**, 8226–8236.
- Turcotte, D.L., 1997. *Fractals and Chaos in Geology and Geophysics*, 2nd edn, Cambridge University Press, Cambridge, UK/New York.
- Twiss, R.J. & Unruh, J.R., 2007. Structure, deformation, and strength of the Loma Prieta fault, northern California, USA, as inferred from the 1989–1990 Loma Prieta aftershock sequence, *GSA Bull.*, **119**(9), 1079–1106.
- Waldhauser, F. & Ellsworth, W.L., 2000. A double-difference earthquake location algorithm: method and application to the northern Hayward Fault, California, *Bull. seism. Soc. Am.*, **90**(6), 1353–1368.
- Wesnousky, S.G., 1988. Seismological and structural evolution of strike-slip faults, *Nature*, **335**, 340–343.
- Wessel, P. & Smith, W.H.F., 1998. New, improved version of the Generic Mapping Tools released, *EOS, Trans. Am. geophys. Un.*, **79**, 579.
- Woodhouse, J.H., 1981. The excitation of long period seismic waves by a source spanning a structural discontinuity, *Geophys. Res. Lett.*, **8**, 1129–1131.

## APPENDIX A: COMPUTATION OF THE SOURCE MECHANISM TENSOR FROM A FAULT PLANE SOLUTION

For a DC source mechanism there are three degrees of freedom since  $\hat{P}_{ij}$  is symmetric, has both trace and determinant constrained to be zero, and has a Euclidean norm of  $\|\hat{P}_{ij}\| = \sqrt{\hat{P}_{ij}\hat{P}_{ij}} = 1$ . The zero determinant corresponds to the requirement that there is always an axis (the null axis) in the direction of which there is zero net deformation. The three parameters of a DC mechanism may also be given in terms of a slip direction given by the rake,  $\gamma$ , on a fault plane given by a strike,  $\varphi$  and dip,  $\delta$ , (Aki & Richards 2002, p. 101). Since we assume that there is no net rotation of the source region during slip, corresponding values of  $\varphi$ ,  $\delta$  and  $\gamma$  define compensating slip in a direction perpendicular to the fault slip along an auxiliary plane perpendicular to the fault plane. Which of the planes is the fault plane and which is the auxiliary plane is arbitrary in the framework of the DC description, producing the so-called ‘fault plane ambiguity’.

The DC focal mechanism orientation (or fault plane solution), given in terms of  $\varphi$ ,  $\delta$  and  $\gamma$ , can be computed by inversion of the pattern of  $P$ - and  $S$ -wave polarities detected by the surrounding seismic stations (Aki & Richards 2002). We convert values of  $\varphi$ ,  $\delta$  and  $\gamma$  to  $\hat{P}_{ij}$  using the following relations, which are adapted from Aki & Richards (2002), p. 112 using  $x_1 = E$ ,  $x_2 = N$  and  $x_3 = up$ :

$$\begin{aligned}
 \hat{P}_{11} &= \frac{1}{\sqrt{2}}(\sin \delta \cos \gamma \sin 2\varphi - \sin 2\delta \sin \gamma \cos^2 \varphi), \\
 \hat{P}_{12} &= \frac{1}{\sqrt{2}}(\sin \delta \cos \gamma \cos 2\varphi + \frac{1}{\sqrt{2}} \sin 2\delta \sin \gamma \sin 2\varphi), \\
 \hat{P}_{13} &= \frac{1}{\sqrt{2}}(\cos \delta \cos \gamma \sin \varphi - \cos 2\delta \sin \gamma \cos \varphi), \\
 \hat{P}_{22} &= -\frac{1}{\sqrt{2}}(\sin \delta \cos \gamma \sin 2\varphi + \sin 2\delta \sin \gamma \sin^2 \varphi), \\
 \hat{P}_{23} &= \frac{1}{\sqrt{2}}(\cos \delta \cos \gamma \cos \varphi + \cos 2\delta \sin \gamma \sin \varphi), \\
 \hat{P}_{33} &= \frac{1}{\sqrt{2}}(\sin 2\delta \sin \gamma).
 \end{aligned}
 \tag{A1}$$

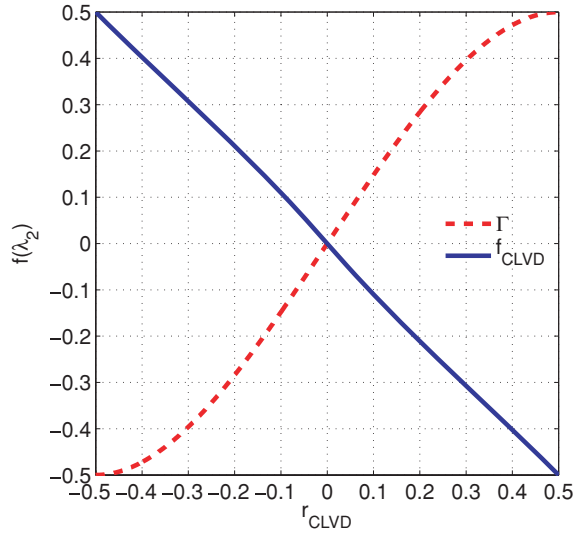


**Figure C1.** Alternative measures of the CLVD component compared to  $r_{\text{CLVD}}$ .

To convert this to the potency tensor, each component should be multiplied by  $P_0/\sqrt{2}$ , while conversion to the moment tensor requires multiplication by  $\sqrt{2}M_0$ , where  $M_0$  is the scalar moment (e.g. Riedesel & Jordan 1989; Aki & Richards 2002). The difference between the position of the  $\sqrt{2}$  in these conversions results from summation over elastic constants when calculating the moment tensor. This is consistent with the relation,  $M_0 = \mu P_0$ , where  $\mu$  is the rigidity.

## APPENDIX B: QUANTIFICATION AND DISPLAY OF THE CLVD COMPONENT

For DC source mechanisms, the eigenvalues of  $\hat{P}_{ij}$  are constrained to be  $\lambda_1 = -1/\sqrt{2}$ ,  $\lambda_2 = 0$  and  $\lambda_3 = 1/\sqrt{2}$ , respectively, such that the eigenvalues for  $P_{ij}$  are  $-P_0/2$ ,  $0$  and  $P_0/2$ . To quantify the non-DC nature of a given summed tensor, we make use of the decomposition into DC and CLVD component tensors (Knopoff & Randall 1970; Julian *et al.* 1998),

$$\begin{aligned} P_{ij} &= P_{ij}^{\text{DC}} + P_{ij}^{\text{CLVD}} \\ &= \frac{1}{\sqrt{2}}(P_0^{\text{DC}} \hat{P}_{ij}^{\text{DC}} + P_0^{\text{CLVD}} \hat{P}_{ij}^{\text{CLVD}}), \end{aligned} \quad (\text{B1})$$

where the eigenvectors of  $P_{ij}$ ,  $\hat{P}_{ij}^{\text{DC}}$  and  $\hat{P}_{ij}^{\text{CLVD}}$  are all the same. The eigenvalues of  $\hat{P}_{ij}^{\text{CLVD}}$  are given by one of two special cases,

$$\lambda_1 = \frac{-2}{\sqrt{6}}, \quad \lambda_2 = \frac{1}{\sqrt{6}}, \quad \lambda_3 = \frac{1}{\sqrt{6}}, \quad (\text{B2})$$

or

$$\lambda_1 = \frac{-1}{\sqrt{6}}, \quad \lambda_2 = \frac{-1}{\sqrt{6}}, \quad \lambda_3 = \frac{2}{\sqrt{6}}.$$

We use a convention that compression is negative, and hence the first case is analogous to uniaxial compression whereas the second is analogous to uniaxial extension.

Since  $\lambda_2 = 0$  for the DC component tensor, a non-zero value of  $P_0^{\text{CLVD}}$  can be interpreted in terms of the value of  $\lambda_2$ , that is the sense of deformation in the direction of the  $B$ -axis. For potency

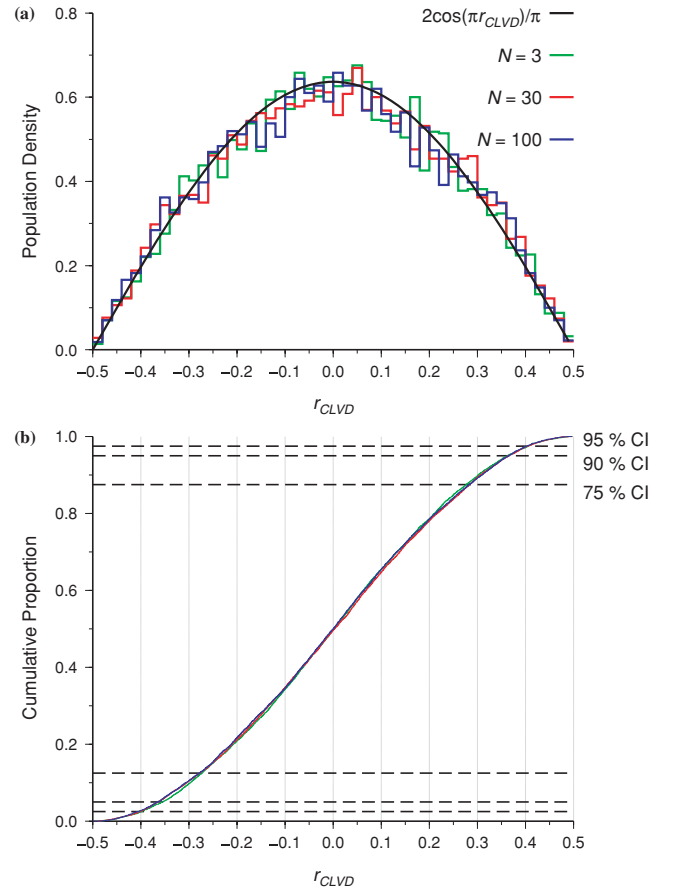


**Figure D1.** (a) Histograms of  $r_{\text{CLVD}}$  based on  $M = 10,000$  simulations where  $N$  randomly oriented DC potency tensors have been summed, shown for  $N = 3$ ,  $N = 30$  and  $N = 100$ . The bins are of width  $\Delta r_{\text{CLVD}} = 0.2$ , and number of simulations in each bin is divided by  $M \Delta r_{\text{CLVD}}$  to normalize the area under each histogram. The function  $(2/\pi) \cos(\pi r_{\text{CLVD}})$  is overlain to illustrate the consistent shape. (b) Cumulative histograms of the same simulations, indicating the 2.5, 5, 12.5, 87.5, 95 and 97.5% values, which correspond to estimates of 75, 90 and 95% confidence intervals for non-randomness given an absolute value of  $r_{\text{CLVD}}$  in a source mechanism summation.

tensors generated by summation of DC potency tensors the CLVD component is described by the sign of  $\lambda_2$  and the relative size of  $P_0^{\text{CLVD}}$ .

$$r_{\text{CLVD}} = \text{sign}(\lambda_2) \frac{P_0^{\text{CLVD}}}{2P_0} = \frac{\sqrt{6}}{2} \lambda_2. \quad (\text{B3})$$

A pure DC tensor is displayed graphically by a beachball plot where the two extensional and compressional regions intersect in the direction of the null axis. The lack of any such intersection indicates deformation in the  $B$ -axis direction, so it can no longer be termed the null axis, and this indicates the presence of a CLVD component. In our method of display, the  $B$ -axis symbol will plot in either a region of compression if  $\lambda_2 < 0$  or extension if  $\lambda_2 > 0$ . For a deviatoric tensor, the areas denoting extension and compression must be equal and the absolute size of the CLVD component is then indicated by size of the smallest angular distance between the  $B$ -axis and the extensional/compressional boundary.

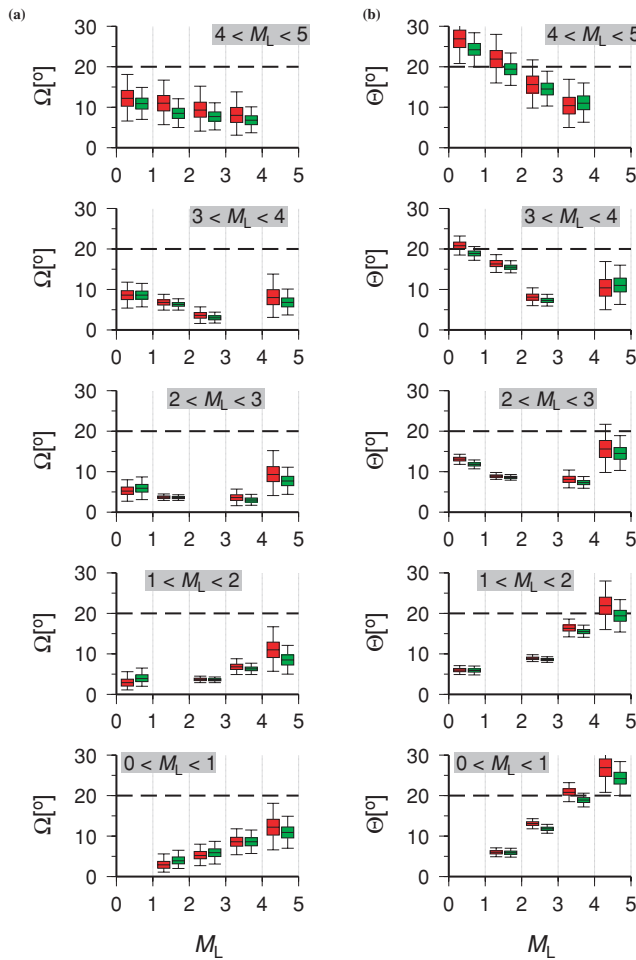


**Figure F1.** The differences between summed tensors for different magnitude bins given by the rotation angles,  $\Omega$  and tensor difference angles,  $\Theta$ . Each plot shows one of the magnitude bins compared with the other four. Red symbols correspond to differences in  $\hat{P}^{TOT}$ , whereas green symbols correspond to differences in  $\hat{P}^{SM}$ . Each plot shows the median, 75% and 95% confidence intervals based on bootstrap analysis of the summed tensor pairs. Confidence intervals are so narrow for differences in  $\hat{P}^{SM}$  in (b) that the box colours are not visible. A dashed line is plotted at  $20^\circ$  for reference.

### APPENDIX C: COMPARISON OF MEASURES FOR THE CLVD COMPONENT

The measure of the CLVD component used in this paper is

$$r_{\text{CLVD}} = \frac{\sqrt{6}}{2} \lambda_2. \quad (\text{C1})$$

In Fig. C1, we compare this to the Gamma-index (Kagan & Knopoff 1985),

$$\Gamma = -(3/2)\sqrt{6}\lambda_1\lambda_2\lambda_3, \quad (\text{C2})$$

and (Giardini 1984),

$$f_{\text{CLVD}} = \frac{-\lambda_2}{\max(|\lambda_1|, |\lambda_3|)}. \quad (\text{C3})$$

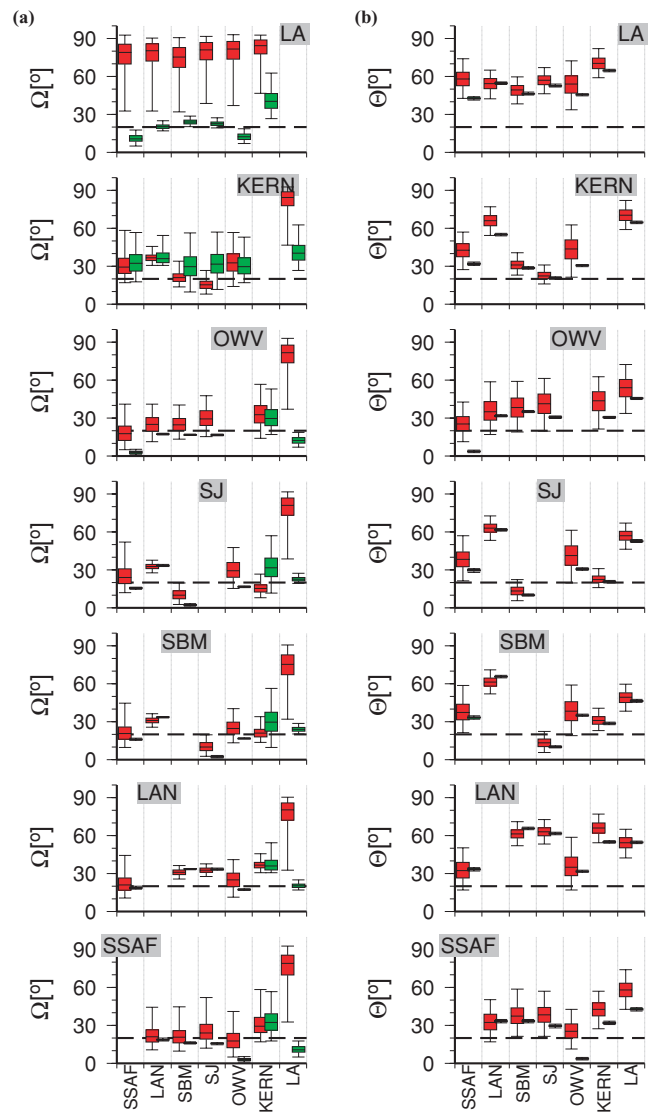


**Figure F2.** The differences between summed tensors for region bins given by the rotation angles,  $\Omega$  and tensor difference angles,  $\Theta$ . Each plot shows one of the regions compared with the other six. The regions are ordered bottom–top/left–right based on the smallest to largest orientation differences,  $\Omega$ , between the  $\hat{P}^{TOT}$  for the region and  $\hat{P}^{TOT}$  for southern California. Red symbols correspond to differences in  $\hat{P}^{TOT}$ , whereas green symbols correspond to differences in  $\hat{P}^{SM}$ . Each plot shows the median, 50 and 95% confidence intervals based on bootstrap analysis of the summed tensor pairs. A dashed line is plotted at  $20^\circ$  for reference.

### APPENDIX D: SIMULATIONS OF RANDOM DC ORIENTATIONS

For summed tensors of DC mechanisms that are uniformly distributed in orientation we can expect that  $r_{\text{CLVD}} = 0$ . This is illustrated in simulations by selecting  $N$  DC potency tensors from a uniform random distribution of orientations using the method of Kagan (2005), and computing the source mechanism summation. The distribution of  $r_{\text{CLVD}}$  based on 10 000 simulations for  $N > 2$  follows a cosine function. We display four example values of  $N$  in Fig. D1(a). The cumulative histograms in Fig. D1(b) indicate that when  $|r_{\text{CLVD}}| \gtrsim 0.35$  for  $\hat{P}_{ij}^{SM}$ , a hypothesis of the CLVD component

being generated by random noise can be rejected at a confidence level of 90%. This implies that although  $|r_{\text{CLVD}}|$  is a measure of fault complexity, it does not represent a degree of randomness.

For  $\hat{P}_{ij}^{\text{TOT}}$  the value of  $r_{\text{CLVD}}$  does not directly compare to these simulations since each potency tensor is weighted by  $P_0/\sqrt{2}$  in the summation. Although  $r_{\text{CLVD}}$  for  $\hat{P}_{ij}^{\text{SM}}$  relates to the amount of complexity in terms of number of events,  $r_{\text{CLVD}}$  for  $\hat{P}_{ij}^{\text{TOT}}$  relates more to the deformation of the considered volume and how significant that complexity is in terms of the overall deformation.

## APPENDIX E: EQUATIONS FOR THE COMPUTATION OF $\Omega$

Based on the eigenvectors,  $\mathbf{e}_1$ ,  $\mathbf{e}_2$  and  $\mathbf{e}_3$ , of the source mechanism tensors, the minimum rotation angle from one orientation of principle strain axes to another is given by (Kuipers 2002)

$$\Omega = \arccos \left[ \frac{\max(\text{Tr}(\mathbf{R}_1), \text{Tr}(\mathbf{R}_2), \text{Tr}(\mathbf{R}_3), \text{Tr}(\mathbf{R}_4)) - 1}{2} \right], \quad (\text{E1})$$

where

$$\begin{aligned} \mathbf{R}_1 &= (\mathbf{e}_1^A, \mathbf{e}_2^A, \mathbf{e}_3^A)(\mathbf{e}_1^B, \mathbf{e}_2^B, \mathbf{e}_3^B)^T \\ \mathbf{R}_2 &= (-\mathbf{e}_1^A, \mathbf{e}_2^A, -\mathbf{e}_3^A)(\mathbf{e}_1^B, \mathbf{e}_2^B, \mathbf{e}_3^B)^T \\ \mathbf{R}_3 &= (\mathbf{e}_1^A, -\mathbf{e}_2^A, -\mathbf{e}_3^A)(\mathbf{e}_1^B, \mathbf{e}_2^B, \mathbf{e}_3^B)^T \\ \mathbf{R}_4 &= (-\mathbf{e}_1^A, -\mathbf{e}_2^A, \mathbf{e}_3^A)(\mathbf{e}_1^B, \mathbf{e}_2^B, \mathbf{e}_3^B)^T. \end{aligned} \quad (\text{E2})$$

## APPENDIX F: QUANTITATIVE COMPARISON OF MAGNITUDE AND REGIONAL SUMMED TENSORS

The difference angles  $\Omega$  and  $\Theta$  for comparisons between the magnitude-based subsets of Section 3.2 and the regional subsets of Section 3.3 are displayed in Figs F1 and F2, respectively. Although both angles are given in degrees, the scales are not analogous, since  $\Theta$  measures an angle between two points on a nine-dimensional hypersphere, whereas  $\Omega$  quantifies an angle of rotation in three-dimensional space.

## APPENDIX G: FURTHER DETAILS ABOUT THE REGIONAL SUBSETS

As shown in Fig. G1, both the number of earthquakes and total potency release for the regions vary significantly. Unlike the comparison for magnitude bins (Fig. 3), log-scaling of the  $y$ -axis is not needed to compare regions, indicating that all regions have a significant contribution to the total summations in Fig. 2. However, the relative differences in column height between the two histograms in Fig. G1 imply that the relative contributions of each region are different for the two summation types,  $P_{ij}^{\text{SM}}$  and  $P_{ij}^{\text{TOT}}$ . For example, the aftershocks of the Landers and Hector Mine earthquakes in region LAN dominate in terms of potency release and thus contribute more to  $P_{ij}^{\text{TOT}}$ , whereas regions OWV and LAN dominate in number and jointly contribute more to  $P_{ij}^{\text{SM}}$ . When considering the entire southern California region, region LA has considerably more influence in potency release than number, whereas the pattern for KERN is opposite. Given the respective significance of reverse and normal faulting in these regions, this may explain why  $r_{\text{CLVD}}$  is positive for  $P_{ij}^{\text{TOT}}$  and negative for  $P_{ij}^{\text{SM}}$  in Fig. 2.

Fig. G2 illustrates the regional differences in temporal seismic behaviour by showing the increase with time of cumulative potency for  $M_L \leq 5$  earthquakes in each region. A constant potency rate is indicated by the straight diagonal line, but all regions progress in a step-like fashion corresponding to the relatively large earthquakes. Regions where large earthquakes occurred (e.g. the 1987 Superstition Hills earthquake in SJ, the 1992 Landers and Big Bear earthquakes in LAN and SBM, the 1994 Northridge earthquake in LA and the 1999 Hector Mine earthquake in LAN) have the strongest divergence from a constant rate of potency release due to the contributions of large aftershocks (the mainshock events mentioned above are not represented in our  $M_L \leq 5$  data). For regions having few notably large earthquakes (SSAF, KERN and OWV), the lines remain closer to the constant potency release rate. A further difference is seen in the curvature of lines after large steps, indicating decay in the number of aftershocks. Although the amount of curvature is affected by the scale of the  $y$ -axis, some regions (e.g. SJ and SSAF) show much less tendency for this curvature than others (e.g. LAN and OWV).

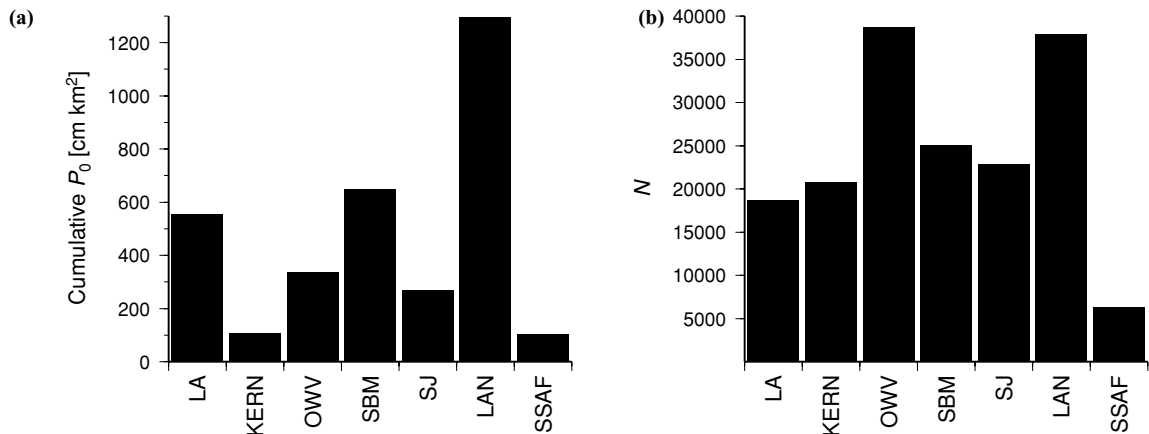


**Figure G1.** (a) Summed scalar potency and (b) total number of events in each of the seven regions shown in Fig. 1.

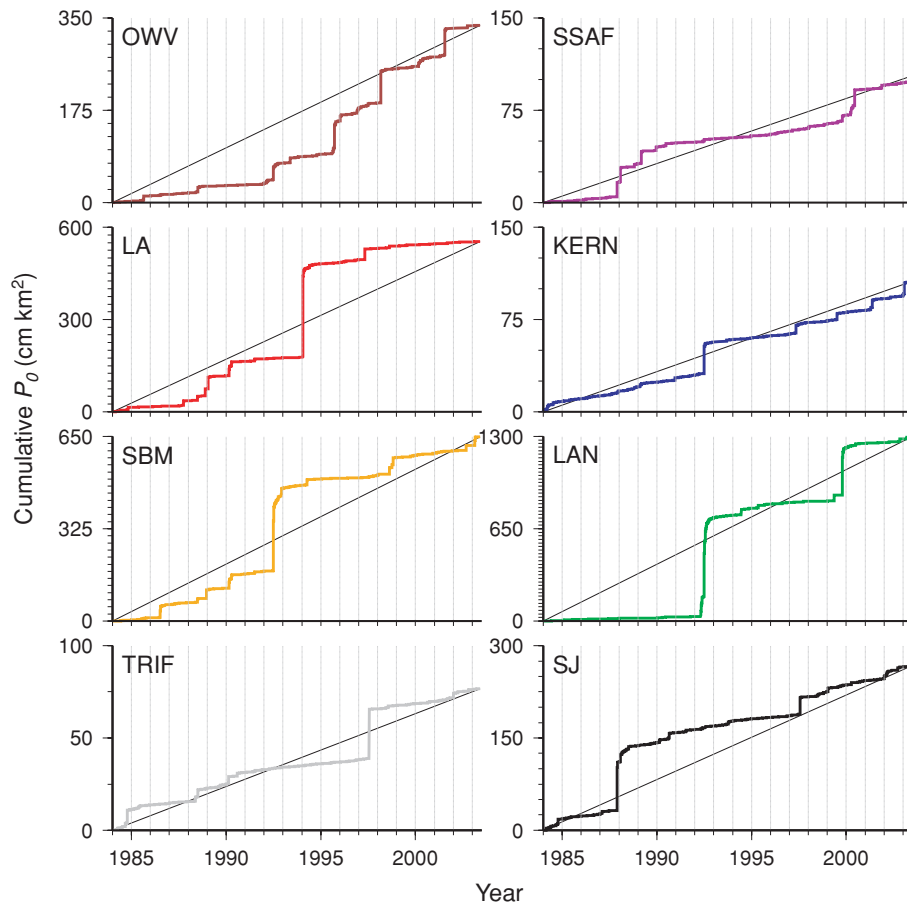


**Figure G2.** Cumulative potency release over the catalogue time interval for  $0 < M_L \leq 5$  earthquakes in each subregion used in this study. Locations of these regions are shown in Fig. 1.